

TIME VARIABILITY OF THE “QUIET” SUN OBSERVED WITH *TRACE*. I. INSTRUMENTAL EFFECTS, EVENT DETECTION, AND DISCRIMINATION OF EXTREME-ULTRAVIOLET MICROFLARES

MARKUS J. ASCHWANDEN, RICHARD W. NIGHTINGALE, TED D. TARBELL, AND C. J. WOLFSON
Lockheed Martin Advanced Technology Center, Solar & Astrophysics Laboratory, Department L9-41, Building 252,
3251 Hanover Street, Palo Alto, CA 94304; aschwanden@lmsal.com

Received 1999 July 27; accepted 2000 January 4

ABSTRACT

The *Transition Region and Coronal Explorer (TRACE)* observed a “quiet-Sun” region on 1999 February 17 from 02:15 UT to 3:00 UT with full resolution (0.5 pixel size), high cadence (125 s), and deep exposures (65 and 46 s) in the 171 Å and 195 Å wavelengths. We start our investigation of the time variability of “quiet-Sun” images with a detailed analysis of instrumental and nonsolar effects, such as orbital temperature variations, filtering of particle radiation spikes, spacecraft pointing drift, and solar rotation tracking. We quantify the magnitude of various noise components (photon Poisson statistics, data digitization, data compression, and readout noise) and establish an upper limit for the data noise level, above which temporal variability can safely be attributed to solar origin. We develop a pattern recognition code that extracts spatiotemporal events with significant variability, yielding a total of 3131 events in 171 Å and 904 events in 195 Å. We classify all 904 events detected in 195 Å according to flarelike characteristics and establish a numerical flare criterion based on temporal, spatial, and dynamic cross-correlation coefficients between the two observed temperatures (0.9 and 1.4 MK). This numerical criterion matches the visual flare classification in 83% of the cases and can be used for automated flare search. Using this flare discrimination criterion we find that only 35% (and 25%) of the events detected in 171 (and 195) Å represent flarelike events. The discrimination of flare events leads to a frequency distribution of peak fluxes, $N(\Delta F) \propto \Delta F^{-1.83 \pm 0.07}$ at 195 Å, which is significantly flatter than the distribution of all events. A sensitive discrimination criterion of flare events is therefore important for microflare statistics and for conclusions on their occurrence rate and efficiency for coronal heating.

Subject headings: Sun: chromosphere — Sun: corona — Sun: transition region — Sun: UV radiation

1. INTRODUCTION

Recent spacecraft observations in soft X-rays (SXR) and extreme ultraviolet (EUV) have established that there is no such thing as a “quiet Sun” when observed with high spatial and temporal resolution. A review on first results (Schrijver et al. 1999) made by the *Transition Region and Coronal Explorer (TRACE)* (Tarbell et al. 1994; Handy et al. 1999), which carries on board an EUV imager with the highest resolution (0.5 pixel size) ever flown, illustrates the omnipresent dynamics of the coronal plasma, evolving virtually anytime at every place on the Sun. The new *TRACE* observations entail coronal loop dynamics (motions, oscillations, weaving, twisting, meandering, rotations, mass flows in loops) as well as chromospheric dynamics (in steep temperature gradients at the footpoints of hot coronal loops due to thermal conduction). Besides the plasma dynamics driven by magnetohydrodynamic processes, there are also the more violent flare processes driven by magnetic reconnection and the kinematics of nonthermal energetic particles. With increased resolution and sensitivity it became feasible to observe smaller flare events, which have been dubbed microflares and nanoflares, because they carry as little as a fraction of 10^{-6} and 10^{-9} in energy compared with the largest observed flare events seen in hard X-rays (HXR). While large flares are generally harbored by active regions of substantial size, microflares were found all over the Sun, in mini-active regions (also called bright points) or in the network of the so-called quiet Sun. The study of microflares and nanoflares is motivated for two reasons: (1) Are the smallest flares governed by the same physical processes as large flares, possibly manifesting the most elementary physical mechanisms involved in flares at large, and (2)

do the statistics of microflares diverge at the low end, leaving open an arbitrarily large energy reservoir to heat the solar corona. Because a smaller spatial scale goes along with a higher occurrence rate, it became feasible to gather large statistics of brightenings with automated algorithms (e.g., Berghmans, Clette, & Moses 1998; Krucker & Benz 1998). The trade-off of large statistics is obviously that less attention is paid to individual events, which is particularly dangerous when the selection criteria of individual events are not well defined or cannot be quantified by sensible criteria. In previous work with event statistics, the selection criteria were mainly based on the discrimination of small events against instrumental noise, using a 3σ significance criterion or the like. However, given the variety of multifaceted plasma motions seen in *TRACE* data, which mimic time variability with high significance, it becomes more intricate to discriminate these phenomena from flare processes. It is the purpose of this study to identify all known sources of (instrumental, nonsolar, and solar) time variability in EUV images and to establish a reliable criterion to discriminate microflare events from other brightenings and dynamic phenomena in the solar corona.

EUV brightenings have been studied primarily with *Skylab*, with the Ultraviolet Spectrometer and Polarimeter (UVSP) on the *Solar Maximum Mission (SMM)*, with the Extreme Ultraviolet Imaging Telescope (EIT) on the *Solar and Heliospheric Observatory (SOHO)*, and now with *TRACE*. Individual microflare events have been studied, e.g., in C IV, at $T = 10^5$ K (Porter et al. 1987; Porter, Fontenla, & Simnett 1995), in Fe IX, at $T = 10^6$ K (Benz & Krucker 1999; Chae et al. 2000; Wang et al. 1999), while larger statistics on EUV brightenings in Fe IX and Fe XII

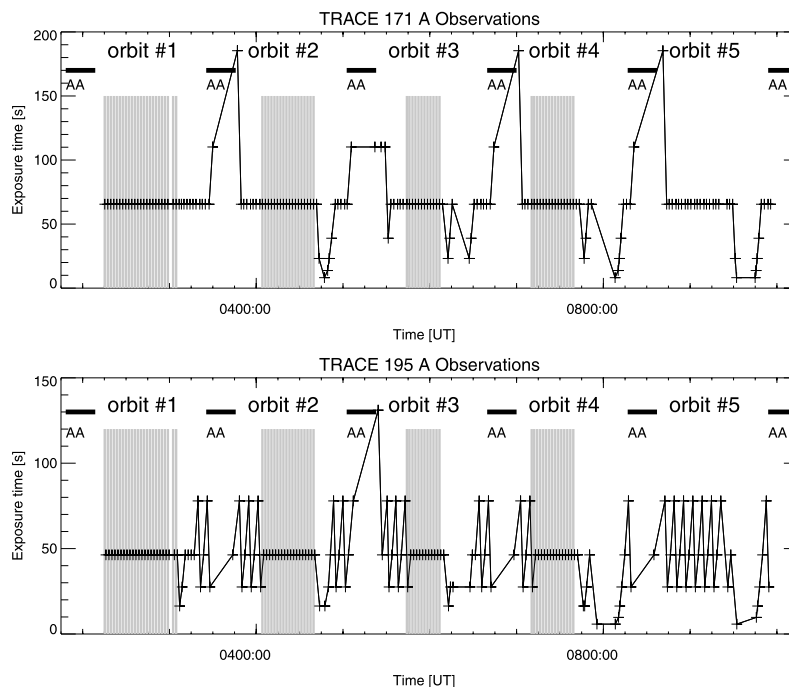


FIG. 1.—Overview of the observing period on 1999 February 17 01:30–10:00 UT. The observing sequence encompasses roughly five spacecraft orbits, which contain blocks (indicated with gray tone) of interleaved wavelength images with a constant cadence (125 s) and constant exposure times (65 s at 171 Å and 47 s at 195 Å). The orbits are interrupted by passages through the South Atlantic Anomaly and radiation belts, where the automatic exposure time changes according to the particle hit rate. Time periods with atmospheric absorption (AA) detected in EUV are indicated with black bars. The analyzed data described in this paper refer to a sequence of 22 interleaved images during the first block at 02:15–03:00 UT.

($T = 1.4 \times 10^6$ K) were reported by Berghmans et al. (1998), Benz & Krucker (1998), and Krucker & Benz (1998). Often it is assumed that microflares are governed by similar physical processes as large flares and thereby have the potential to provide heating mechanisms for the corona at large. While recent statistical studies have been performed with $\approx 5''$ ($2''.5$ pixel size) spatial resolution (using *SOHO*/EIT), the unprecedented resolution of $\approx 1''$ ($0''.5$ pixel size) with *TRACE* bears the potential to resolve up to an order of magnitude more microflares and thus may reveal crucial statistics at the low end of the frequency distribution that is most relevant for coronal heating.

The plan of the paper is the following: Using some dedicated observations of the “quiet Sun” while pointing to a coronal hole (§ 2) we analyze first all instrumental effects that are important to filter out unwanted artificial time variability and we characterize the data noise (§ 3). We perform then a variability analysis with a grid of 4×4 macropixels and localize macropixels with significant variability (§ 4). We develop a pattern recognition code that

assembles significant spatiotemporal patterns to events (§ 5). We then inspect all events and apply a phenomenological classification to sort out flare events from other dynamic transients and then establish an objective “numerical flare criterion” that can be used for automated flare search (§ 6). We discuss the physical definition of flare events (§ 7.1) and compare the obtained EUV frequency distributions of flare events with those from other wavelengths (§ 7.2). Conclusions are summarized in § 8.

2. OBSERVATIONS

A special observing sequence was performed with the *Transition Region and Coronal Explorer (TRACE)* (Tarbell et al. 1994; Handy et al. 1999) to study the variability of the quiet Sun, requiring long exposures with the highest cadence possible, as well as two wavelengths to provide temperature and emission measure diagnostics. The observation took place on 1999 February 17, 01:30–10:00 UT, extending over 8.5 hr. During this time interval, a total of 173 full-resolution images (with 1024×1024 pixels and

TABLE 1
TIMES OF ANALYZED TRACE 171 Å AND 195 Å OBSERVATIONS

Orbit Number	Wavelength (Å)	Start Time (1999 Feb 17 UT)	End Time (1999 Feb 17 UT)	Exposure Time (s)	Cadence (s)	Number of Images
1	171	02:15:16.0	02:58:55.0	65.5	125.0	22
	195	02:16:06.0	02:59:45.0	46.3	125.0	22
2	171	04:06:21.0	04:41:43.0	65.5	125.0	18
	195	04:05:07.0	04:40:20.0	46.3	125.0	18
3	171	05:45:56.0	06:08:47.0	65.5	125.0	12
	195	05:46:47.0	06:09:38.0	46.3	125.0	12
4	171	07:14:17.0	07:43:23.0	65.5	125.0	15
	195	07:13:03.0	07:42:09.0	46.3	125.0	15

pixel size of 0".5) were recorded at a wavelength of 171 Å and 168 interleaved full-resolution images at a wavelength of 195 Å. Owing to an automatic exposure control mechanism to protect the lifetime of the CCD, the exposure times vary from 1.7 to 185 s during our observing sequence (Fig. 1). The most frequent exposure times are 65.536 s at 171 Å (141 images) and 46.340 s at 195 Å (99 images). In order to have a constant rms noise, we select images with identical exposure times in each wavelength, i.e., those with the most frequent exposure times. Further, we require a constant cadence for each pair of 171 and 195 Å images, which is most frequently a cadence of 125 s. The total time sequence of 8.5 hr includes approximately five spacecraft orbits, containing four blocks with continuous cadences of 125 s and constant exposure times, interrupted by time gaps with variable (mostly shorter) exposure times due to entry of the spacecraft in South Atlantic Anomaly (SAA) and regions of enhanced particle precipitation from the Earth's radiation belt. The start and end times of these four selected time blocks are listed in Table 1, containing 22, 18, 12, and 15 image pairs during the four orbits, i.e., a total of 67 images in each wavelength. In this first paper we restrict ourselves on the analysis of the first orbit.

3. INSTRUMENTAL AND NONSOLAR EFFECTS

The primary purpose of this data analysis is to discriminate instrumental, nonsolar, and solar effects that contribute to time variability in the observed *TRACE* images, a quantification of their magnitude, and their correction in the data in order to provide accurate statistics of solar transients and microflaring. Standard software used for processing of *TRACE* data can be found in Solar SoftWare (SSW) libraries (Freeland & Handy 1998), which run in IDL software environment.

3.1. Flat-Fielding and Correction of Bad Pixels

A first step in processing the original data is to subtract an image of the dark pedestal (Analog-Digital-Converter [ADC] offset), which is done with the standard software provided by the *TRACE* team (IDL procedure `TRACE_PREP`, status 1999 April). For our set of images during the first orbit, the pedestal and dark current value of the images is 87.96 data numbers (DN), with a standard deviation of $\sigma_{\text{dark}} = 1.32$ DN. The basic data number unit of 1 DN corresponds to an amplifier gain of 12 electrons DN^{-1} (for default amplifier A; Handy et al. 1999), where each electron corresponds to a detected photon that passes into the lumogen coating (that fluoresces at visible wavelength when hit by UV and EUV photons).

Besides subtraction of the pedestal value, a further correction is flat-fielding for bad pixels (with efficiency less than 100%). Currently, flat-field correction is not applied to any of the *TRACE* images.

3.2. Orbital Temperature Variations

The *TRACE* spacecraft is in a Sun-synchronous polar orbit of 600×650 km at an inclination of $97^\circ 8'$, following roughly the solar terminator. This orbit had uninterrupted sunshine during the first 7 months after launch (1998 April–October), followed by a 3 month period of partial eclipse (1998 November–1999 January). In 1999 February, shortly after the eclipse period, EUV absorption and variation of the spacecraft temperature was detected, probably caused by the varying geometry of the Earth shine and albedo.

Absorption of EUV emission reduces the observed flux. The orbit predict data indicate significant atmospheric absorption during the time intervals 01:48:18–02:08:43 UT, 03:25:25–03:45:49 UT, 05:02:33–05:22:55 UT, 06:39:41–07:00:00 UT, 08:16:49–08:37:06 UT, and 09:53:57–10:14:11 UT (marked with black bars in Fig. 1). These intervals approximately correspond to the time intervals when the automatic exposure control switched to longer exposure times at 171 Å (see Fig. 1). However, atmospheric absorption seems not to be severe during the time interval selected for analysis here (marked with gray tone labeled orbit 1 in Fig. 1).

Temperature changes in the spacecraft can vary the pedestal value and noise of the readout current of the CCD camera and thus can introduce variability in difference images. To quantify this effect we plot a histogram $N(f)$ of the flux f (in DN counts per exposure time per pixel) for a sequence of 22 images, shown in Figure 2 for both wavelengths. We fit a Gaussian to the peak of the logarithmic distribution $N(f)$, which indicates the most likely flux level of the static quiet Sun. We find a shift of the Gaussian peak by $\Delta f \approx +3$ DN during this orbit in both wavelengths, varying from 30.4 to 33.1 DN at 171 Å and from 19.3 to 22.6 DN at 195 Å (Fig. 2 [left]). This systematic increase of the pedestal value (Fig. 2 [top right]) seems to be related to a systematic temperature decrease during this part of the orbit (Fig. 2 [bottom right]). The offset Δf_{orbit} of the count rate is not exactly proportional to the temperature change of the CCD camera because the used temperature sensor (at the CCD camera) is displaced from the electronics most sensitive to the orbital temperature changes and thus introduces a hysteresis effect. We correct for this temperature-related variability by subtraction of the time-dependent peak offset $\Delta f_{\text{orbit}}(t)$, using the values shown in Figure 2 (top right).

3.3. Correction of Hot Pixels

Contrary to the bad pixels, which show up in the white-light flat field and indicate a permanent underefficiency (probably due to fabrication artifacts), there are also temporary “hot pixels,” which produce a high readout current that remains high for some period of time, probably because some electrons are not properly flushed out after a CCD readout. These hot pixels are easy to detect because they appear persistently over some period of time, mostly isolated in single pixels, which show much higher counts than the surrounding pixels. In our time sequence of 22 images we detect such hot pixels by comparing the counts of each pixel f_{ijk} with the average of the nearest neighbors (in a 3×3 area) in the preceding and following time steps (t_{k-1} , t_{k+1}), i.e.,

$$f_{ijk}^{\text{neighbor}} = \frac{1}{16} [\sum f_{ij'k-1} + \sum f_{ij'k+1}] \quad (1)$$

$$i' = i - 1, i, i + 1, \quad j' = j - 1, j, j + 1, \quad i'j' \neq ij.$$

We identify hot pixels above a threshold factor $q_{\text{thresh}} = 1.5$ (or 1.15), compared with the count level in the neighbored pixels, i.e.,

$$f_{ijk}^{\text{hot}} > q_{\text{thresh}} f_{ijk}^{\text{neighbor}}. \quad (2)$$

The nearest spatial neighbors at time step t_k are ignored because, if f_{ijk} is a pixel with a cosmic-ray hit, its spatial neighbors are also affected at time t_k but unlikely at times

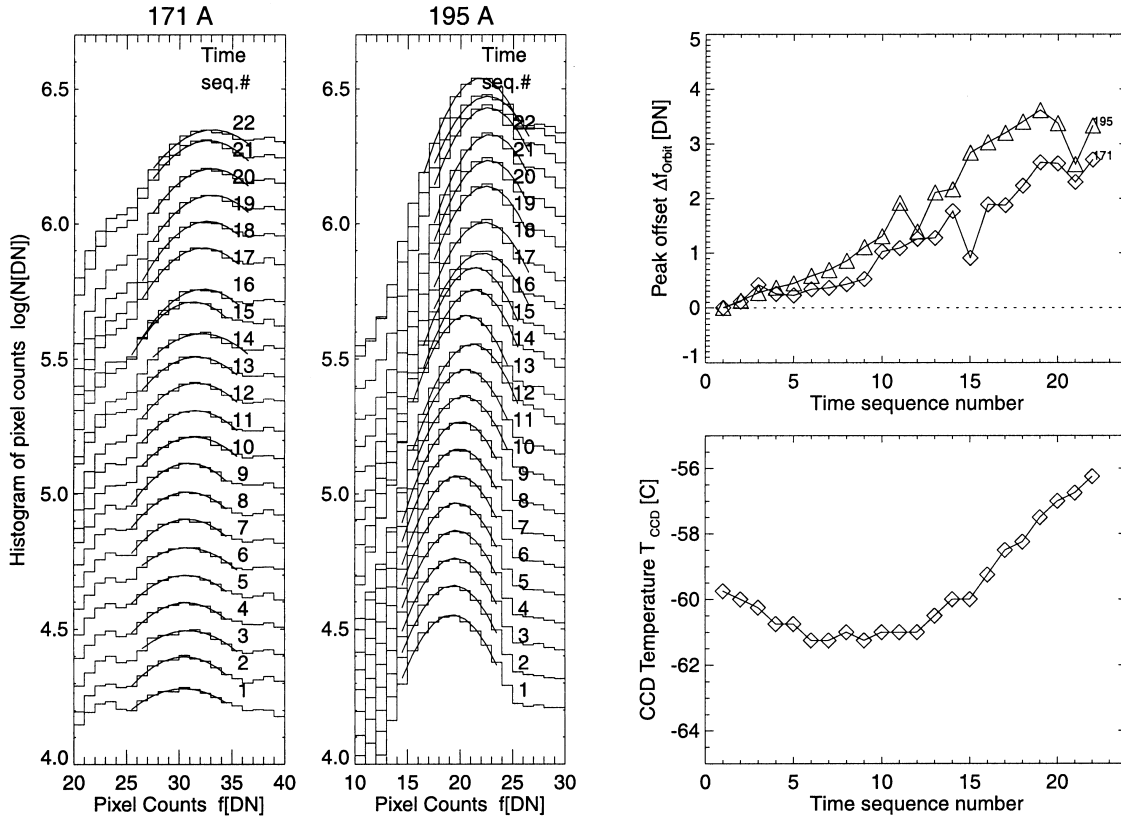


FIG. 2.—Distribution of counts (DN) in the sequence of 22 analyzed images is shown around the most frequent values (≈ 30 DN at 171 \AA and ≈ 20 DN at 195 \AA) in the histograms on the left-hand side. A Gaussian is fitted to the logarithmic distribution near each peak to evaluate a time-dependent offset Δf_{orbit} of the most frequent DN value. This offset Δf_{orbit} (top right) is found to be correlated with the orbital variation of the spacecraft temperature T_{CCD} (bottom right).

t_{k-1} and t_{k+1} . Requiring a persistence of 50% in time (i.e., contiguously present in 50% of the time series), we find a total of 989 hot pixels (0.09%) in our time series at 171 \AA and a total of 1195 hot pixels (0.11%) at 195 \AA inside the illuminated circular area of the CCD camera. These hot pixels f_{ijk}^{hot} are corrected by replacing them with the average neighbor value $f_{ijk}^{\text{neighbor}}$.

3.4. Filtering of Particle Radiation Spikes

The 600 km altitude of the *TRACE* orbit leads through locations of the South Atlantic Anomaly (SAA) and near-polar latitudes of enhanced auroral particle precipitation from the radiation belt. During the passage of such locations, particle hits (mainly from ≈ 1 MeV electrons) on the CCD camera become occasionally quite severe, in particular in long-exposure images as used here (affecting $\lesssim 10^5$ pixels out of the 10^6 in each image). Fortunately the signatures of cosmic-ray hits are easily recognizable as single-pixel spikes that are about 1–2 orders of magnitude higher than the rms fluctuations of the quiet Sun. These single-pixel spikes are generally surrounded by a ring of next-neighbor pixels that are also enhanced to some fraction due to the *jpeg* data compression scheme. A standard procedure is provided in the software of the *TRACE* team, called *TRACE_UNSPIKE*, which replaces a spiky pixel (with an excess flux of 15% relative to the local median value) by this median value (defined by the nearest eight neighbors in a 3×3 pixel area around the spike). This procedure can be applied iteratively 3 times to clean up the ringlike residuals around the spike caused by the *jpeg* data compression algorithm. Because this standard procedure turned out to be

insufficient for most of the long-exposure images here (since the number of noisy pixels increases proportionally to the exposure time for a constant hit rate), we develop a more efficient filter (called *TRACE_UNSPIKE_TIME*) that uses a combination of spatial and temporal nearest neighbor pixels. The average of the nearest two temporal neighbors is

$$f_{ijk}^{\text{time}} = \frac{1}{2}[f_{i,j,k-1} + f_{i,j,k+1}]. \quad (3)$$

A spiky pixel f_{ijk}^{spike} is detected if its counts exceed the temporal average by a factor $q_{\text{thresh}} = 1.5$ (or 1.15), i.e.,

$$f_{ijk}^{\text{spike}} > q_{\text{thresh}} f_{ijk}^{\text{time}}, \quad (4)$$

and is then corrected with the temporal average f_{ijk}^{time} . An example of this cleaning algorithm is shown in Figure 3, enlarged from a subfield of 80×80 pixels. Two strong cosmic-ray hits seen in this subfield have diameters of 3–4 pixels, which are properly cleaned after one iteration. The histogram (Fig. 3 [right]) shows a mean value of ≈ 20 DN for the background. The filter criterion with a factor 1.5 removes all spikes with $\gtrsim 10$ DN excess above the temporally averaged background. This algorithm removes also cosmic-ray streaks of sufficient intensity (with an excess of $\gtrsim 10$ DN). A potential danger is that narrow loops that have an appearance almost indistinguishable from linear streaks could be filtered away. We investigated the cleaning efficiency with various thresholds and found an optimum in a range of $q_{\text{thresh}} \approx 1.15 \dots 1.50$. Lower values $q_{\text{thresh}} < 1.15$ have the tendency to “overclean” by rounding sharp edges of small-scale structures, while higher values $q_{\text{thresh}} > 1.5$ leave cosmic-ray spike residuals greater than 10 DN in the data.

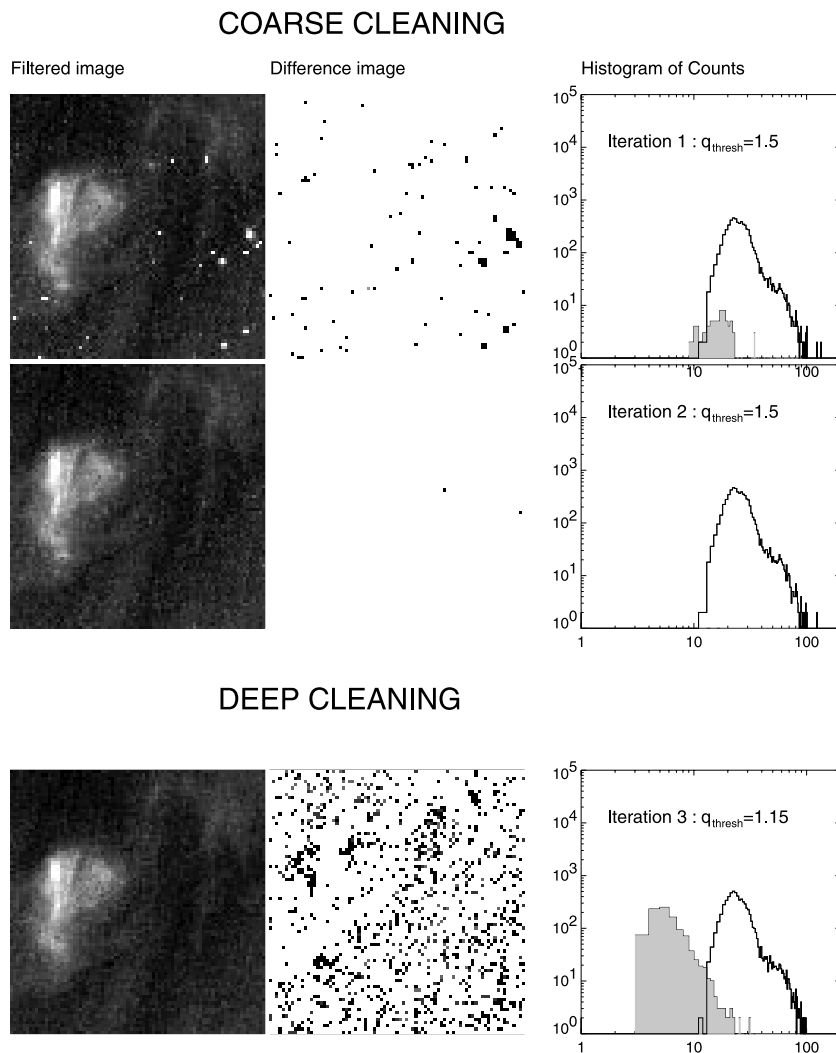


FIG. 3.—Filtering of spikes caused by cosmic-ray hits is illustrated for a subfield (pixel range $x = 375:455$, $y = 545:625$) of the first image of our analyzed data set, recorded on 1999 February 17 02:15:16 UT at 195 Å. The original image is shown top left, and the filtered image after subsequent iterations in the same column, all shown on a linear gray scale with a range of 10–100 DN. The difference images in the middle column display the differences between subsequent iterations of our cleaning algorithm, shown on an enhanced linear gray scale with a range of 0–5 DN. The histograms in the right panels show the pixel value distributions (in DN) of the images (*white histograms*) and difference images (*gray histograms*). The first two iterations (“coarse cleaning”) are performed with a threshold of $q_{\text{thresh}} = 1.5$, while the third iteration (“deep cleaning”) uses a threshold of $q_{\text{thresh}} = 1.15$.

We perform the cleaning of our time sequence of 22 images (in both wavelengths) in two steps, applying first two iterations with a *coarse cleaning* threshold of $q_{\text{thresh}} = 1.5$, followed by a third iteration of *deep cleaning* with a lower threshold $q_{\text{thresh}} = 1.15$. The efficiency of this cleaning algorithm after each iteration is illustrated in Figure 3. The total number of corrected noisy pixels amounts to $\approx 6\%$ – 10% per image. The lower percentage applies to quiet times of the orbit, while the higher percentage applies to passages through radiation belts. These numbers of cosmic-ray hits apply to an exposure time of 65 and 47 s at the two wavelengths, yielding a cosmic-ray hit rate of $\approx (1\text{--}2) \times 10^3$ particle hits on the CCD camera per second.

3.5. Correction of Solar Rotation

The *TRACE* telescope was pointing to $58''$ west and $133''$ south of the Sun center during this observing run, without tracking the solar rotation. In order to obtain cospatial time series in each image pixel, we transform the image coordinates into a corotating coordinate system, which has

a relative velocity of

$$v_{\text{rot}} = \frac{2\pi R_{\odot}}{T_{\text{syn}}} = 1.8557 \text{ km s}^{-1} = 0''.00256 \text{ s}^{-1} \quad (5)$$

at Sun center, with $R_{\odot} = 696,000$ km and a synodic rotation period of $T_{\text{syn}} = 27.2753$ days. The correction between two subsequent images (with a cadence of 125 s and a pixel size of $0''.5$) amounts therefore to 0.64 pixels, accumulating to 13.44 pixels between the first and last (22d) image of our first data set. The nonoverlapping 13 pixel wide strip is discarded in our further analysis.

3.6. Spacecraft Pointing Drift

The pointing of the *TRACE* spacecraft is controlled by an Image Stabilization System (ISS) that is expected to provide a pointing accuracy of $5''$ – $10''$. A source of disturbance is the quad-shutter, which causes residual changes of $0''.5$. Another factor is temperature changes, which causes some flexing between the guide telescope and the main

TRACE telescope, which can cause drifts in the order of $\pm 1''$ during an orbit.

We measure the pointing accuracy by cross-correlations (using the IDL procedure `GET_CORREL_OFFSETS` from the SSW software) in four image quadrants inside the circle of the unvignetted CCD field of view. We plot the mean of the drift in the x - and y -directions and their standard deviation (among the four image quadrants) in Figure 4, for both the 171 and 195 Å image time series. The correlation offset in 195 Å shows a much larger standard deviation among the four quadrants, probably because some are dominated by single microflares with some dynamic evolution and centroid shifts of order $10''$. The 171 Å image shows a much smaller scatter among the four quadrants, probably because there are more numerous features visible that average out the individual eigenmotions. For correction of the pointing drift in the data we use the smoothed pointing offsets (smoothed with a boxcar of five time steps; see the thick solid lines in Fig. 4). The smoothed pointing drift in the x -direction is then found to have the following extrema: $+0.87$ pixels at time step 7 (after 15 minutes) and -1.96 pixels at time step 22 (after 44 minutes). The smoothed pointing drift in the y -direction has the following extrema: $+0.00$ pixels at time step 0 and -3.11 pixels at time step 22 (after 44 minutes). The maximum drift of the pointing during our first orbit is therefore only 4.2 pixels or $2''.1$. We correct the data by bilinear interpolation in a coordinate grid that is shifted by these pointing offsets.

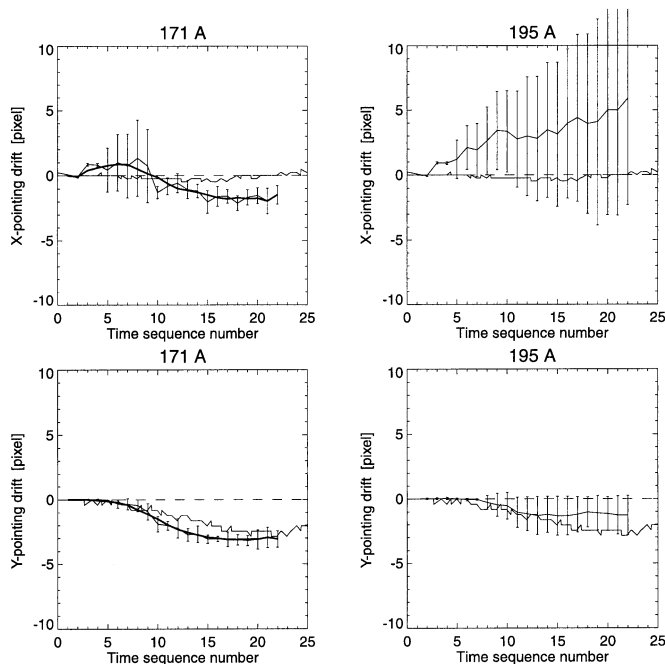


FIG. 4.—Spacecraft pointing drift is shown from cross-correlations measurements with respect to the first image of the time sequence during 02:15–03:00 UT. The thin line and error bars indicate the mean and standard deviations among cross-correlations performed in four image quadrants (inscribed to the circle of the illuminated CCD camera field of view). The thick line represents a five-point sliding average. The pointing drift in the x -direction is shown in the top panels for both wavelengths and in the y -direction in the bottom panels. Note that the larger scatter of the pointing in 195 Å is probably caused by the centroid motion of individual microflares. A prediction of the pointing drift based on temperature sensor information is shown also (*ragged line*), which is very consistent with the drift measured from cross-correlations in the y -direction, but predicts less drift in the x -direction.

Additional information on the pointing drift is obtained from temperature sensors on the telescope spider structure. Tarbell found from other *TRACE* data (1998 October 14, 8–12 UT) a good correlation between temperature changes measured by temperature sensor 6 on the metering tube B (spider nr 0) and the pointing drift in the north-south direction,

$$\Delta y_{\text{pointing}} \approx -\frac{4}{3} \Delta T_{\text{No.6}} \text{ (pixels)}, \quad (6)$$

and between temperature changes $T_{\text{No.6}}$ (in centigrade) measured by temperature sensor 7 on the metering tube B (spider nr +120) and the pointing drift in the east-west direction,

$$\Delta x_{\text{pointing}} \approx -\frac{2}{3} \Delta T_{\text{No.7}} \text{ (pixels)}. \quad (7)$$

The predicted pointing drifts are shown in Figure 4, which match the values found from cross-correlation shifts in the y -direction but predict less in the x -direction. Therefore, we have an independent corroboration of the pointing correction in the y -direction.

3.7. Data Noise

The rms noise in the data is composed of a number of instrumental components, which we estimate in the following, and are compiled in Table 2, including photon Poisson noise, electronic readout noise, data digitization, data compression, dark-current noise, and residual noise from cosmic-ray hits. Various noise components are specified in units of data numbers (DN), which are accumulated over a fixed exposure time of 65.5 s (at 171 Å) and 46.3 s (at 195 Å) in our data set.

Let us first estimate the photon statistics. The quantum efficiency of the *TRACE* CCD is 0.08–0.09 electrons photon $^{-1}$ (Handy et al. 1999, Table V), which is relatively low owing to the lumogen coating in front of the CCD (to boost the EUV sensitivity). Thus, about 1 photon is effectively detected from 11 incident photons. Each detected photon produces an electron in the silicon pixel, which is amplified and produces an Analog-Digital Converter (ADC) readout with a conversion factor of 12 electrons DN $^{-1}$. From the histograms of the most frequent pixel values (see Fig. 2) we find a typical background level of $f_{\text{quiet}} \approx 30$ DN at 171 Å and $f_{\text{quiet}} \approx 20$ DN at 195 Å. Assuming Poisson statistics for the incoming detected photons, we expect therefore a photon noise of $\sigma_{\text{photon}} = (f_{\text{quiet}} \times 12)^{1/2}/12 = 1.58$ DN at 171 Å (and 1.29 DN at 195 Å).

There is a readout noise with an rms of 20 electrons for the *TRACE* CCD camera (Handy et al. 1999, Table IV), which converts into $\sigma_{\text{readout}} = 20/12 = 1.67$ DN.

The digitization of the data numbers allows us only to store the data with an accuracy of ± 0.5 digits and thus introduces an uncertainty of $\sigma_{\text{digit}} = 0.5$ DN.

The accuracy of the stored data is further reduced by the *jpeg* data compression algorithm, which allows us to reduce the large data amount significantly. During our observation, a lossless compression algorithm was used, which reduces the accuracy of the compressed data almost unnoticeably. For “lossless” compression, only 7%–9% of the pixels are found to have an error of ± 1 DN. Therefore, the average noise due to lossless compression averaged over the entire image is $\sigma_{\text{compress}} \lesssim 0.1$ DN.

The subtraction of the dark current with a pedestal value (§ 3.1) as well as the subtraction of a temperature-dependent

TABLE 2
DATA NOISE COMPONENTS OF TRACE 171 Å AND 195 Å IMAGES (WITH 65 AND 46 s s EXPOSURE TIME)

Noise Component	171 Å	195 Å	171 Å	195 Å
	Single Pixel (DN)	Single Pixel (DN)	4 ² Macropixel (DN)	4 ² Macropixel (DN)
A.				
Quiet-Sun background counts F_{quiet}	30	20	30	20
Photon noise $\sigma_{\text{photon}}(C)$	1.58	1.29	0.40	0.32
Readout noise σ_{readout}	1.67	1.67	0.42	0.42
Digitization noise σ_{digit}	0.50	0.50	0.13	0.13
Lossless compression σ_{compress}	0.10	0.10	0.03	0.03
Pedestal/Dark current σ_{dark}	1.32	1.32	0.33	0.33
Integer subtraction σ_{subtract}	0.70	0.70	0.17	0.17
Spike residuals σ_{spikes}	4.50	3.00	1.12	0.75
Predicted data noise σ_{noise}	5.29	4.00	1.32	1.00
B.				
Number of valid macropixels			38,622 (100%)	38,622 (100%)
Predicted significant pixels $N(>3 \sigma_{\text{noise}})$			20,902 (54%)	4794 (12%)
Measured significant pixels $N(>3 \sigma_{\text{rms}})$			18,859 (49%)	5857 (15%)

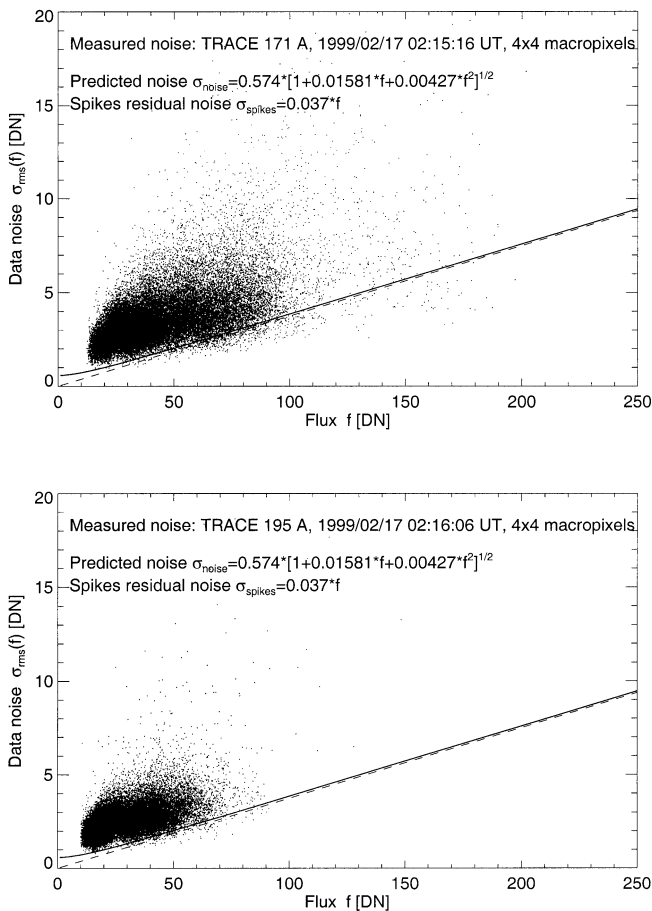


FIG. 5.—Theoretical data noise model is shown as function of the pixel flux (*thick line*), $\sigma_{\text{rms}}(f)$ (see eq. [9]). The most dominant noise source, i.e., residuals of cosmic-ray spikes, is shown also (*dashed line*). This predicted noise level is compared with the rms fluctuations measured in 4×4 macropixels (*dots*), which contain besides instrumental data noise also real solar fluctuations. Note that the lower envelope of the measured data noise agrees well with the theoretical noise model.

background variation (§ 3.2) are done in integer DN and thus add two further digitization uncertainties, $\sigma_{\text{subtract}} = 0.5 \times \sqrt{2} = 0.7$ DN.

The largest contribution to data noise results from the removal of cosmic-ray hits or from the residuals left by the cleaning process. In our cleaning algorithm we set a threshold of 15% (deep cleaning), which translates into residuals of $\sigma_{\text{spikes}}(f_{\text{quiet}}) = f_{\text{quiet}}(q_{\text{thresh}} - 1) = 4.5$ DN at 171 Å and 3.0 DN at 195 Å. We find that $\approx 10\%$ of all image pixels were hit by cosmic rays. Even if all these pixels were properly cleaned, we expect that about the next four nearest neighbors are enhanced above some level, which are not further cleaned if they have an excess below the thresholds. Thus we estimate that $\approx 40\%$ neighbor pixels have cosmic-ray residuals comparable to the threshold. We assume therefore as worst case that most of the pixels have residuals somewhat below the cleaning threshold.

Combining all these uncertainties, assumed to be independent, we expect a total rms data noise of

$$\sigma_{\text{noise}}^2(f) = \sigma_{\text{photon}}^2(f) + \sigma_{\text{readout}}^2 + \sigma_{\text{digit}}^2 + \sigma_{\text{compress}}^2 + \sigma_{\text{dark}}^2 + \sigma_{\text{subtract}}^2 + \sigma_{\text{spikes}}^2(f), \quad (8)$$

which amounts to $\sigma_{\text{noise}}(f_{\text{quiet}}) = 5.29$ DN at 171 Å and $\sigma_{\text{noise}}(f_{\text{quiet}}) = 4.00$ DN at 195 Å. In the following data analysis we will use macropixels, which include spatial averages of 4×4 pixels. These macropixels represent thus averages of $4^2 = 16$ values, which have an rms noise that is a factor of $\approx \sqrt{16} = 4$ smaller. The predicted data noise in these macropixels is therefore $\sigma'_{\text{noise}} = \sigma_{\text{noise}}/4 = 1.32$ DN at 171 Å and $\sigma'_{\text{noise}} = \sigma_{\text{noise}}/4 = 1.00$ DN at 195 Å.

Numerically, the combined data noise defined in equation (8) for macropixels with a length of $n_{\text{macro}} = 4$ can be expressed as

$$\sigma_{\text{noise}}(f) = 0.574[1 + 0.016f + 0.00426f^2]^{1/2} \approx 0.037f \text{ (DN)}. \quad (9)$$

For fluxes $f \gtrsim 20$ DN the combined data noise is dominated by the spike residual noise σ_{spikes} . Thus, for count rates above the quiet-Sun background of $f > f_{\text{quiet}}$, the data noise can accurately be approximated by the spike residual noise component alone, i.e., $\sigma_{\text{noise}}(f > f_{\text{quiet}}) \approx \sigma_{\text{spikes}}(f) = (0.15f)/4 = 0.037f$. The dependence of the theoretically predicted data noise $\sigma_{\text{noise}}(f)$ as function of the count rate f is shown in Figure 5 (*solid line*), together with the approximation of the spike residual component (*dashed line*). A significance limit of $f > 3 \sigma_{\text{noise}}$ should establish a reliable confidence limit between fluctuations owing to instrumental effects and those that can be believed to be of solar origin.

4. VARIABILITY ANALYSIS

4.1. Spatial Variability in Macropixels

The spatiotemporal variability can be analyzed with full spatial and temporal resolution at the expense of a poor signal-to-noise ratio or with reduced spatial and/or temporal resolution with the advantage of a higher signal-to-noise ratio, which allows detection of significant structures on smaller flux levels. For an initial variability analysis we reduce the spatial resolution by a factor of 4 and thus improve the signal-to-noise ratio by a factor $\sqrt{4^2} = 4$. We refer to these rebinned units as macropixels, which have a spatial scale of $4 \times 0''.5 = 2''$ (with a time resolution of 125 s).

We rebin the full-resolution data cubes from 1999 February 17 02:15–03:00 UT in 171 Å and 195 Å (each of size $1024 \times 1024 \times 22$) to $4 \times 4 \times 22$ macropixels and obtain 256×256 time profiles with a length of 22 time steps. We consider only the central circular part of the image that is free of vignetting, i.e., within a radius of 500 pixels from the image center at (512, 512). Because we are interested only in the variability of the quiet Sun, we discard also 25% of the southern part of the images where a bright active region was observed. This leaves us with a fraction 61.4% of the image pixels, yielding 38,622 valid macropixels or time profiles.

The combination of 16 single pixels to 1 macropixel provides the advantage of measuring empirically the rms fluctuations in each macropixel by calculating the mean and standard deviation of the 16 flux values, $\sigma_{\text{rms}}(f)$. We plot these measured rms values of the 38,622 macropixels of the first image of our analyzed *TRACE* image sequence in Figure 5 as function of the average flux values f of each macropixel. The scatterplot shows that the bulk of these rms values lies above the theoretically estimated data noise $\sigma_{\text{noise}}(f)$ (*solid line* in Fig. 5), which forms a sharp lower cutoff, $\sigma_{\text{noise}}(f) \lesssim \sigma_{\text{rms}}(f)$. The few data points below the theoretical noise curve must belong to macropixels that are free of cosmic-ray hits, for which our noise model overestimates the data noise. On the other side, the majority of data points has a somewhat larger rms, which is likely to be associated with true variability of the solar flux. Thus the theoretical noise estimate $\sigma_{\text{noise}}(f)$ seems to represent a reliable model of the instrumental data noise and nonsolar data fluctuations.

4.2. Significance of Variability in Macropixels

We characterize the time variability in the simplest way, just by measuring the maximum flux change f , defined by the difference of the maximum and minimum in each time series $f_{xy}(t)$ of the 38,622 macropixel locations xy , i.e.

$$\Delta f_{xy} = \max [f_{xy}(t)] - \min [f_{xy}(t)]. \quad (10)$$

We show a histogram $N(f)$ of these fluctuations Δf_{xy} in Figure 6, displayed on a linear flux scale, for both wavelengths (Fig. 6 [*top*]: 171 Å; Fig. 6 [*bottom*]: 195 Å; *thin-lined histograms*). The flux units Δf are given in counts per integration time, i.e., DN/65.6 s for 171 Å and DN/46.3 s for 195 Å.

There are now two independent ways to estimate the significance of these variabilities. One possibility is to use the measured rms (of spatial variations) in the macropixels to establish an upper limit of the local data noise level, measured at the minimum of each time series, $\sigma_{\text{rms}}(f_{\text{min}})$. Requiring a significance level above 3, which has a probability of only 0.27% for random fluctuations in a normal distribution, we can define the significance level based on the empirically measured rms fluctuations,

$$N_{\sigma} = \frac{\Delta f}{\sigma_{\text{rms}}(f_{\text{min}})} \geq 3. \quad (11)$$

We find a total of 18,859 macropixels (49%) that have a significant time variability ($N_{\sigma} \geq 3$) in the 171 Å data cube. A smaller number of 5857 macropixels (15%) with significant time variability is found at 195 Å. The distributions of these significant pixels with $N_{\sigma} \geq 3$ are shown in Figure 6 (*thick-lined histogram*). The fraction $q(\Delta f)$ of these significant pixels to all pixels is also shown in Figure 6 (histograms with gray scale), indicating that undersampling (say $\leq 75\%$) occurs for flux changes of $\Delta f \lesssim 10$ DN in both wavelengths.

A second independent way to estimate the significance of time variability in the macropixels is to use the theoretically calculated data noise $\sigma_{\text{noise}}(f)$ (eq. [9]). The statistical uncertainty of a flux difference $\Delta f = (f_{\text{max}} - f_{\text{min}})$ measured in a time series $f(t)$ with a maximum $f_{\text{max}} \pm \sigma_{\text{noise}}(f_{\text{max}})$ and a minimum $f_{\text{min}} \pm \sigma_{\text{noise}}(f_{\text{min}})$ is expected to have a standard deviation of

$$\sigma_{\Delta f}^{\text{theo}}(f_{\text{max}}, f_{\text{min}}) = [\sigma_{\text{noise}}^2(f_{\text{max}}) + \sigma_{\text{noise}}^2(f_{\text{min}})]^{1/2}. \quad (12)$$

In analogy with the empirical significance criterion (eq. [11]), we define a theoretical significance criterion,

$$N_{\sigma}^{\text{theo}} = \frac{\Delta f}{\sigma_{\Delta f}^{\text{theo}}} \geq 3. \quad (13)$$

Examining the significance of the time variabilities Δf in the 38,622 macropixels with this theoretical criterion $N_{\sigma}^{\text{theo}} \geq 3$ we find a total of 20,902 time series (54%) that fulfill the significance criterion in the 171 Å data. This is only a 5% difference to the result we found from the empirical significance criterion. Also, we find a smaller number of 4794 significant macropixels (12%) at 195 Å, which differs only by 3% from what we found with the empirical significance criterion. The corresponding distributions $N(\Delta f)$ of significant pixels as function of the variable flux Δf are also shown in Figure 6 (*half-thick-lined histogram*). The good agreement between the two significance criteria corroborates our model of the data noise (§ 3.7), and we can use either the empirical or theoretical significance criterion to separate data noise from real solar variability in the macropixels. Relying on this data noise model, we can also predict the data noise in single pixels, which cannot be measured from the rms as in macropixels.

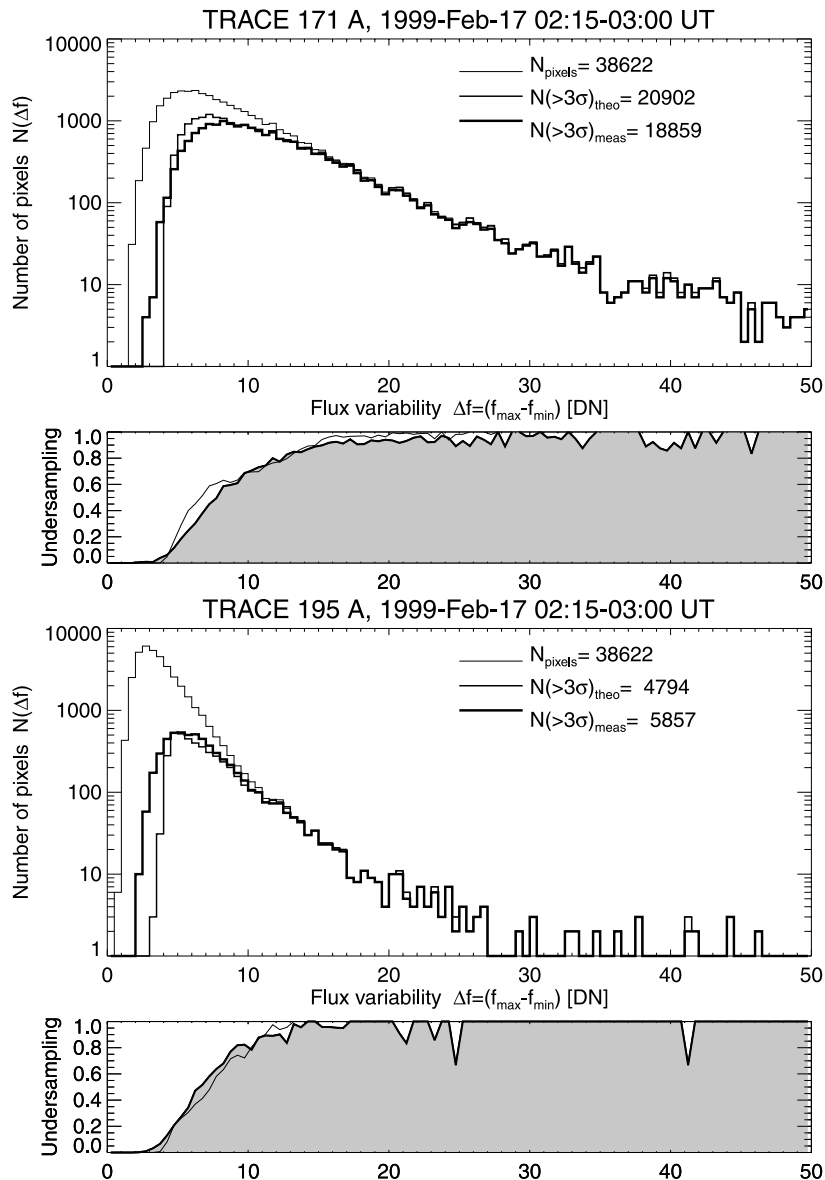


FIG. 6.—Distribution of the flux variability $N(\Delta f)$ measured from the difference $\Delta f = f_{\max}(t) - f_{\min}(t)$ in the time series of each macropixel (*thin histogram*). A subset of macropixels with fluctuations $\Delta f > 3\sigma$ (eq. [11]) is represented with a thick solid line, while the predicted distribution based on the theoretical noise model (eq. [13]) is shown with a half-thick solid line. Note that both the predicted and measured distribution of significant pixels agree within a few percent. The undersampling factor of significantly varying pixels is given as function of the flux Δf with a gray-colored function, indicating undersampling at $\Delta f \gtrsim 10$ DN.

4.3. Spatial Map of Variability

In Figure 7 we show spatial maps of macropixels with significant variability ($N_{\sigma} \geq 3$), overlaid on the first image of our time sequence of 171 and 195 Å images. The selected field of view that encompasses the 38,622 macropixels is outlined in Figure 7. The maps show that the southern half of the image is dominated by some large-scale structures that are associated with the bright active region in the south (eclipsed from our field of view). The eastern half of the 171 Å image shows numerous small-scale structures with dark intrusions, similar to the “moss” structure seen generally in active regions by *TRACE*, which has a more diffuse appearance in the hotter ($T_e \approx 1.4$ MK) 195 Å image. Pixels with significant variability in the 171 Å image encompass all bright structures associated with the active region and the mosslike structures. No significant variability is seen only in

some of the darkest areas in the coronal hole in the northern section. While 49% of the area in the 171 Å image (Fig. 7a) shows significant variability, this is the case in only 15% of the area in the 195 Å image (Fig. 7b), mainly in areas associated with small regions that would be called “bright points” in *Yohkoh* nomenclature.

5. PATTERN RECOGNITION

5.1. Event Definition

In order to obtain statistics of independent events, we have to combine variable macropixels that vary temporally and spatially in a coherent way. Let us define such a coherent spatiotemporal pattern as an *event*, if it fulfills the following two criteria:

1. The spatial extent of an *event* is defined by a cluster of

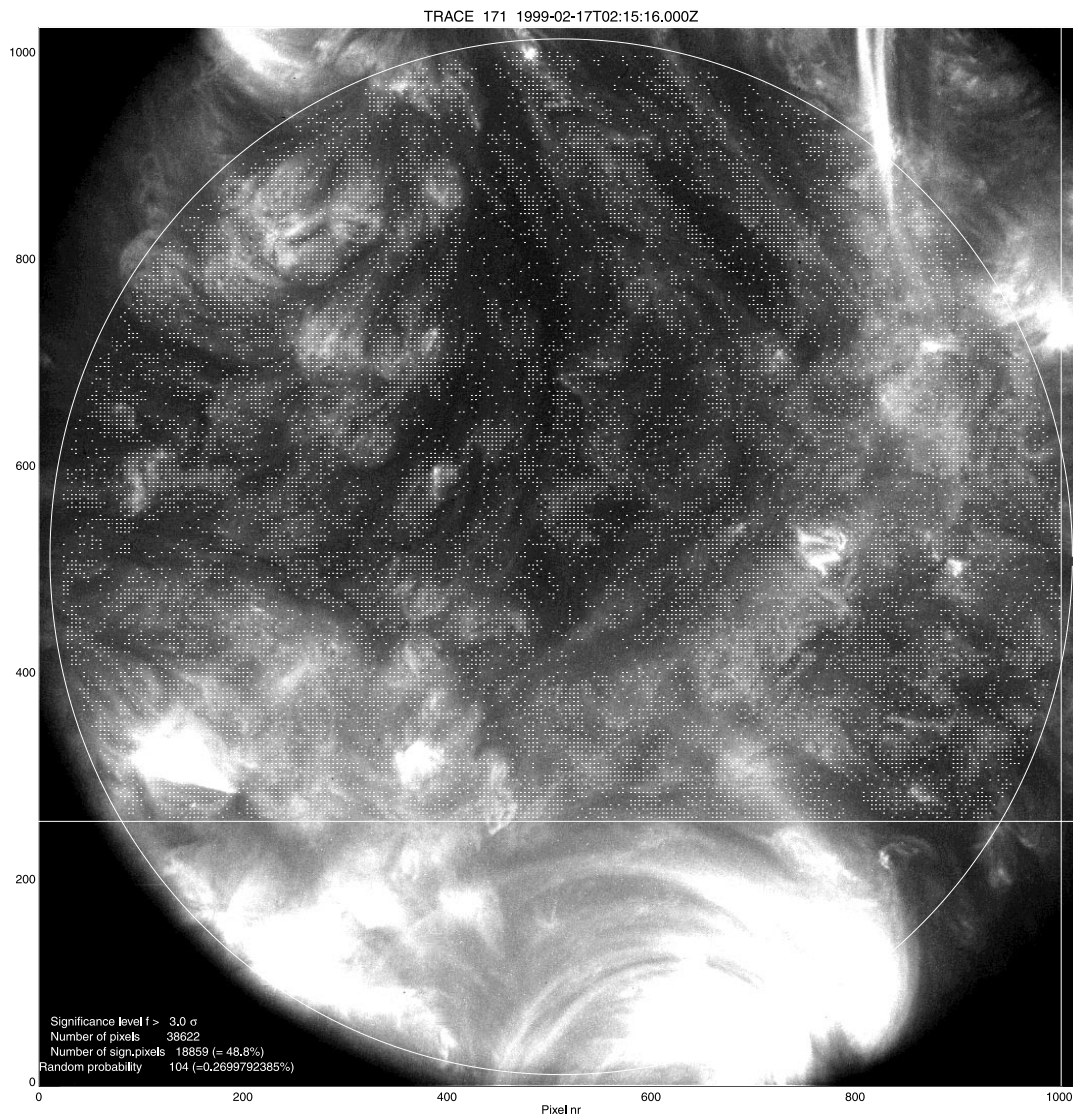


FIG. 7a

FIG. 7.—Spatial distribution of significantly varying macropixels (*dots*) is overlaid on the first 171 Å and 195 Å image of our time series. Note that 18,859 (48.8%) macropixels are variable in 171 Å, while 5857 (15.2%) macropixels are variable in 195 Å, above a significance level of $N_\sigma > 3$.

spatially neighbored pixels that exhibit coherent time variability with a significance of $\geq 3\sigma$. The spatial neighborhood of a pixel includes the nearest 4 side pixels as well as the nearest 4 diagonal pixels (i.e., up to 8 nearest neighbor pixels. (For our 4×4 macropixels the distance to the next nearest neighbors amounts to $1 \dots \sqrt{2} \times 2'' = 1400 \dots 2000$ km.)

2. Coherent time variability inside the spatial pattern of an *event* is defined by the temporal coincidence of the peak flux $\Delta f(t)$ (of all spatial macropixels of an event) within a certain tolerance limit. For our time series with a cadence of $\Delta t = 125$ s, we choose a tolerance limit of $\pm 1\Delta t \approx 2$ minutes.

This event definition is similar to that used by Krucker & Benz (1998), which instead restrict to 4 nearest spatial neighbor pixels (in each iteration step) and to a time tolerance limit of $\pm 0\Delta t$.

5.2. Event Search Algorithm

We design a numeric algorithm for spatiotemporal

pattern recognition in our three-dimensional data cubes $f(x, y, t)$ (with 256×256 spatial macropixels and 22 time steps):

1. In each time series of the 38,622 valid macropixels, we determined the flux maximum $f_{\max}(x, y)$, the flux minimum $f_{\min}(x, y)$, the peak time $t_{\text{peak}}(x, y)$, the minimum time $t_{\min}(x, y)$, and the significance $N_{\text{sigma}}(x, y)$ (eqs. [10] and [11]). The flux variability is characterized by the differences $\Delta f(x, y) = f_{\max}(x, y) - f_{\min}(x, y)$ and is sorted in decreasing order.

2. Starting with the pixel with the largest flux variability $\Delta f(x, y)$ we search for the spatially nearest neighbors with significant variability ($N_\sigma \geq 3$) and coincidence of the peak time within $t_{\text{peak}}(x, y) \pm \Delta t$. The spatial search path is propagated in all four directions ($+x, +y, -x, -y$) until rows and columns are found in all four directions where no pixel meets the significance and coincidence criteria. This cluster defines an event and all macropixels belonging to this event are eliminated for future events.

3. The remaining spatial macropixels with significant

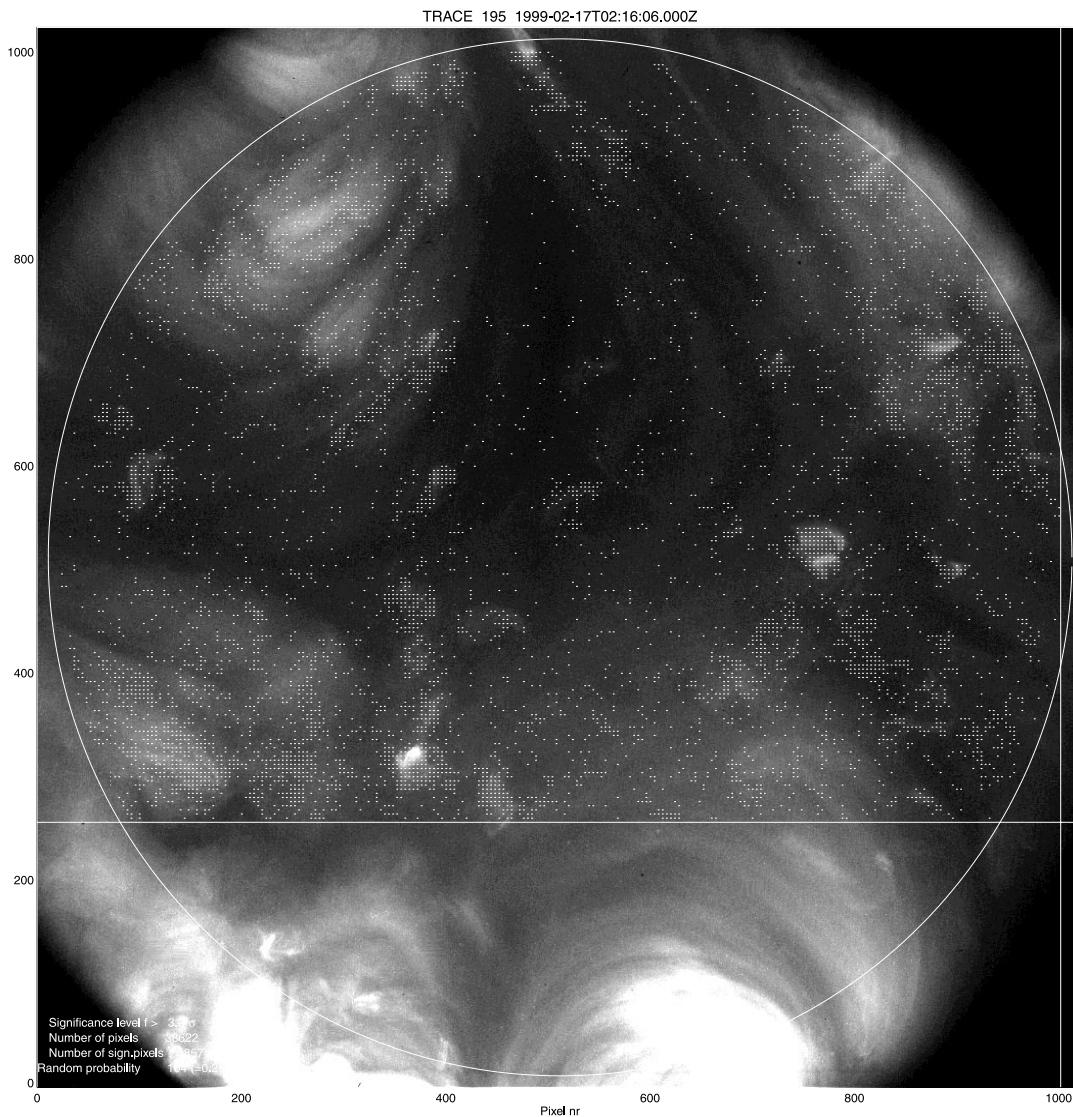


FIG. 7b

variability ($N_\sigma \geq 3$) are re-sorted according to the largest flux variability $\Delta f(x, y)$ and the algorithm iteratively repeats steps 2 and 3 to search for further events until no significant pixel is left. Events with a size of 1 single macropixel are ignored.

A consequence of this spatiotemporal algorithm is that only one (the largest) event is detected in each time series (or in a given macropixel). However, recurrent activity in a particular area generally does not peak exactly at the same location (within the $2''$ of a macropixel), and thus this restriction should not effect the event statistics.

Some examples of detected events are shown in Figure 8, showing the first 12 events (with the highest variability) detected in the 195 \AA data cube. The pixels that exhibit a significant variability ($N_\sigma \geq 3$) during their time series are marked with cross symbols in Figure 8 (corresponding to the dot symbols in Fig. 7b), overlaid on the flux maps $F(x, y)$ (contours in Fig. 8). Those pixels that have been clustered to a common event (marked with diamonds in Fig. 8) have all a coincident temporal peak in their time series within $\pm 1\Delta t$, while the other pixels with cross symbols not

included in the cluster peak at another time (during the analyzed interval of 45 minutes).

The statistics reveals 3131 events in the 171 \AA data and 904 events in the 195 \AA data, recorded within a field of view of ≈ 6.5 squared (or 1.33% of the solar surface) during 45 minutes. This corresponds to an event rate of about 100 events s^{-1} at 171 \AA and 25 events s^{-1} at 195 \AA on the total solar surface.

5.3. Geometry of Events

We characterize the spatial structure of each event with the following geometric parameters: the center position x_c, y_c , the half-axes ($l/2, w/2$), and orientation angle α of an encompassing ellipse. The orientation angle of the ellipse is derived from a linear regression fit $y(x)$ (or $x(y)$ in case of $|\alpha| > 45^\circ$) of the x, y coordinates of the significant macropixels that belong to the event. The spatial coordinates of these macropixels are then rotated by an angle $-\alpha$ into a coordinate system that is co-aligned with the ellipse axes, where the length l and maximum width w is measured from the extrema in the rotated coordinates.

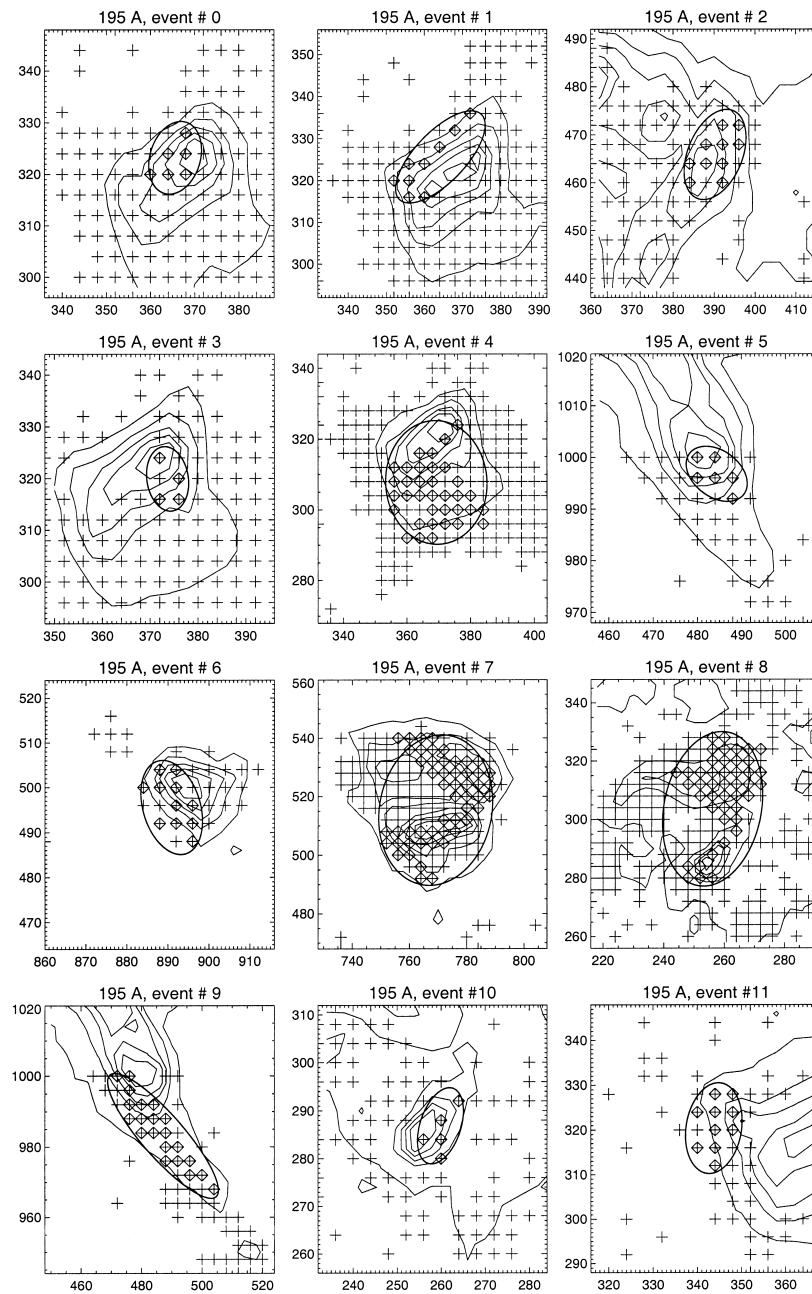


FIG. 8.—Spatial clustering of the pattern recognition code is illustrated for the 12 largest events on 1999 February 17, 02:15–03:00 UT. The contours outline local EUV intensity maps around the detected structures. The crosses mark the positions of macropixels with significant variability ($N_\sigma > 3$). The spatiotemporal pattern algorithm starts at the pixel with the largest variability, which is located at the center of each field of view, and clusters nearest neighbors if they fulfill the time coincidence criterion ($t_{\text{peak}} \pm 1\Delta t$). These macropixels that fulfill the time coincidence criterion define an event, marked with diamonds, and encircled with an ellipse. Each macropixel that is part of an event, is excluded in subsequent events. Note that events 0, 1, 3, and 11 belong to the same active region, where the four zones have peaks at different times and thus make up four different events.

We show the distribution of spatial scales in Figure 9. The spatial lengths l of events cover a range of $l \approx 3\text{--}25$ Mm, while the widths cover a range of $w \approx 1.5\text{--}10$ Mm. Note that the lower cutoffs of event size scales are given by the minimum area requirement of two macropixels ($l > 3$ Mm, $w > 1.5$ Mm). The distribution of lengths l can be described by an exponential distribution $N(l) \propto \exp(-l/2.8$ Mm) (Fig. 9 [top]) for both wavelengths. There is a typical ellipticity ratio of $l/w \approx 2$.

5.4. Event Flux F

So far we considered flux changes $\Delta f = f(t_{\text{max}}) - f(t_{\text{min}})$ of variable pixels. A scatterplot of the averaged pixel flux Δf

per event is shown in Figure 9 (bottom panel) as function of the spatial scale l of the event, which shows no obvious correlation. The total flux of an event is therefore expected to scale approximately with the area of the event.

We define now the total flux of an event, integrated over the area of all N pixels that belong to an event,

$$F(t) = \sum_{i=1}^N f(x_i, y_i, t) = \sum_{i=1}^{N_{\text{MP}}} \langle f(x_i, y_i, t) \rangle N_{\text{bin}}^2, \quad (14)$$

where $\langle f \rangle$ represents the average flux per macropixel and N_{MP} represents the number of macropixels with significant variability, with a binning factor of $N_{\text{bin}} = 4$ for macro-

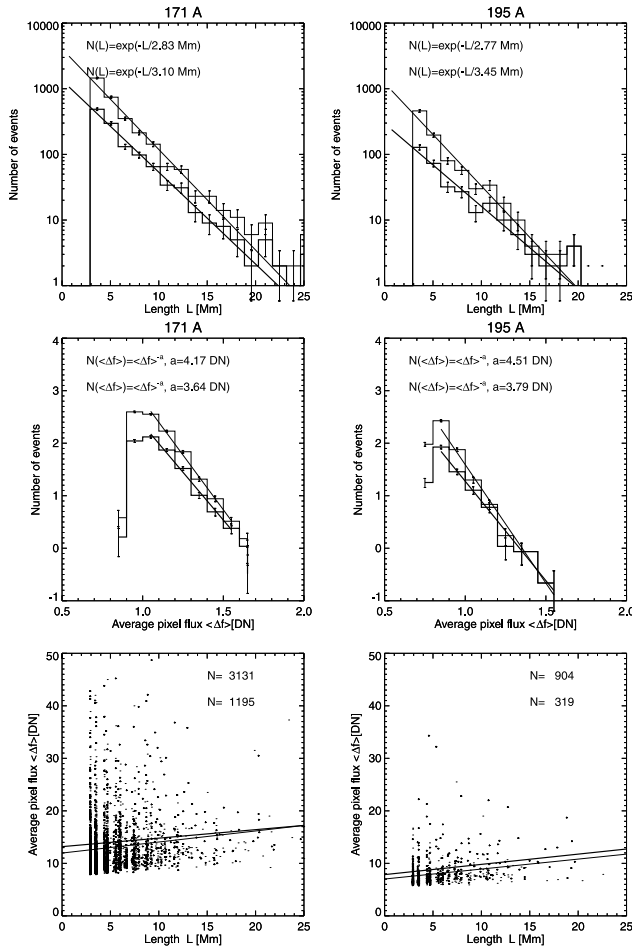


FIG. 9.—Distribution of event length scales L (Mm) (*top panels*), average fluxes per pixel Δf (*middle panels*), and scatterplot between these two parameters (*bottom panels*), for 171 Å (*left-hand column*) and 195 Å (*right-hand column*). The distribution $N(L)$ can approximately be characterized with an exponential function, and the distribution $N(\Delta f)$ with a power law. There is no obvious correlation between L and Δf , suggesting that the total flux of an event scales roughly with the area of an event. The secondary distributions (*thick lines*) represent the selection of flare events.

pixels here. Since we are interested only in flux changes, we subtract the event-unrelated background. Estimating the background level from the minimum time t_{\min} in the time series $f(t)$ [recall that we determined the peak time t_{peak} and minimum time t_{\min} from the time series of the macropixel with the largest variability $\Delta f(t)$; § 4.2], we define an event net flux $\Delta F(t)$

$$\Delta F(t) = F(t) - F(t_{\min}) \quad (15)$$

and denote the peak flux of the event shortly by

$$\Delta F = \Delta F(t = t_{\text{peak}}) = F(t_{\text{peak}}) - F(t_{\min}). \quad (16)$$

The expected standard deviation or the rms noise of an event is then

$$\sigma_F = \left[\sum_i^N \sigma_f^2 \right]^{1/2} = \left[\sum_i^{\text{NMP}} \sigma_{f,\text{MP}}^2 \right]^{1/2}. \quad (17)$$

Similarly we quantify the error bars $\sigma_f(t)$ in time profiles from the net flux $F(t)$ of an event. The significance level N_σ^E of an event is then defined by

$$N_{\text{sigma}}^E = \frac{\Delta F}{\sigma_F}. \quad (18)$$

The event flux ΔF scales approximately with the event area $A = \sum_{i=1}^N \Delta x \Delta y$. This is expected if the average flux per pixel, $\langle \Delta f \rangle$, does not depend much on the event size. In Figure 9 we show the distribution of mean pixel fluxes (Fig. 9 [*middle*]) and a scatterplot of this mean pixel flux $\langle \Delta f \rangle$ with the length scale l of events (Fig. 9 [*bottom*]). There is indeed no statistically significant correlation between these two parameters. The event flux is therefore approximately proportional to the event area, $\Delta F \propto A$.

6. DISCRIMINATION OF MICROFLARES

We are approaching now the final steps of our flare search procedure, i.e., the discrimination of solar flare events from other time-variable phenomena that are not related to flares, microflares, or nanoflares. A sensible discrimination criterion is extremely important for establishing statistics and frequency distributions of flares at flux levels near the detection threshold because the smallest flare events are most numerous there and dominate the statistics. Statistics on flare events have been published in previous studies based on visual inspection of a few of the very largest events of a data set (usually $\lesssim 10$) that represent only the “top of the iceberg,” without verifying flare characteristics of the huge number of smaller flares (typically $\lesssim 10^2$ – 10^4 events). In this study we check each individual event not only by visual inspection but also establish a numerical flare definition that can be used as a criterion for automated discrimination against other nonflaring phenomena.

6.1. Phenomenological Classification of Events

We perform a visual inspection of all 904 events detected in the 195 Å data in form of figures as shown in Figures 10a–10c, containing from both wavelengths: (1) the time sequence of 22 co-aligned images in 171 and 195 Å with a field of view twice the event diameter (Fig. 10 [*top panels*]), (2) sum images (summed from five images around the peak time t_{peak}) to improve the signal-to-noise ratio (Fig. 10 [*bottom left-hand panels*]), (3) a contour plot of the sum image (Fig. 10 [*bottom second left-hand panels*]), (4) a difference image (of the sum image at the peak time t_{peak} minus the sum image at the minimum time t_{\min}), and (5) time profiles of the integrated flux $F(t)$ of variable pixels inside the event boundaries, including error bars of the combined rms noise (Fig. 10 [*bottom right-hand panels*]).

We perform a tentative classification of these 904 events into five categories by visual inspection of their spatial morphology: (1) flare events with loop structures, (2) events with amorphous structures, (3) events associated with “mosslike” structures, (4) events with no recognizable structure or noisy data, and (5) events with obvious bad data. We define these five classes and give examples in the following.

1. *Flare events*.—An example of a typical (micro-) flare event is shown in Figure 10a (event 8). A flare shows typically one or multiple loop structures that brighten up (impulsive phase) in both the 171 and 195 Å wavelengths and then cool down with an exponential-like decay curve (postflare phase). The time profiles in both wavelengths are often well correlated, but the wavelength with the cooler plasma (i.e., $T_e \approx 0.9$ MK at 171 Å) peaks a few minutes later than the hotter plasma (i.e., $T_e \approx 1.4$ MK at 195 Å). The spatial structure of a loop displays a curved segment when seen from a favorable perspective but often shows just

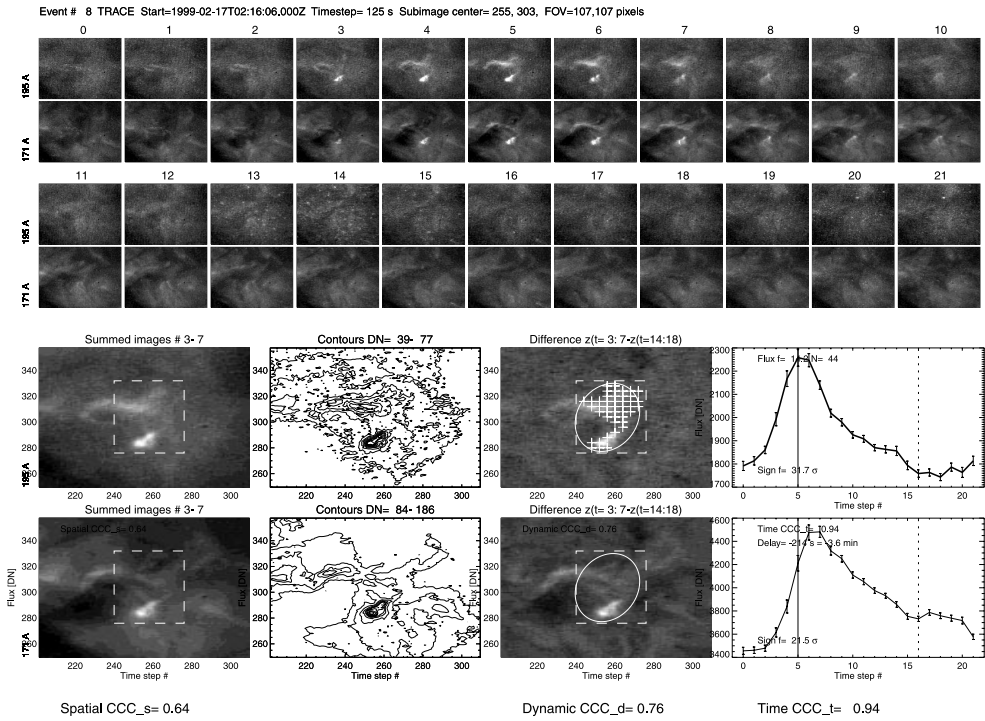


FIG. 10a

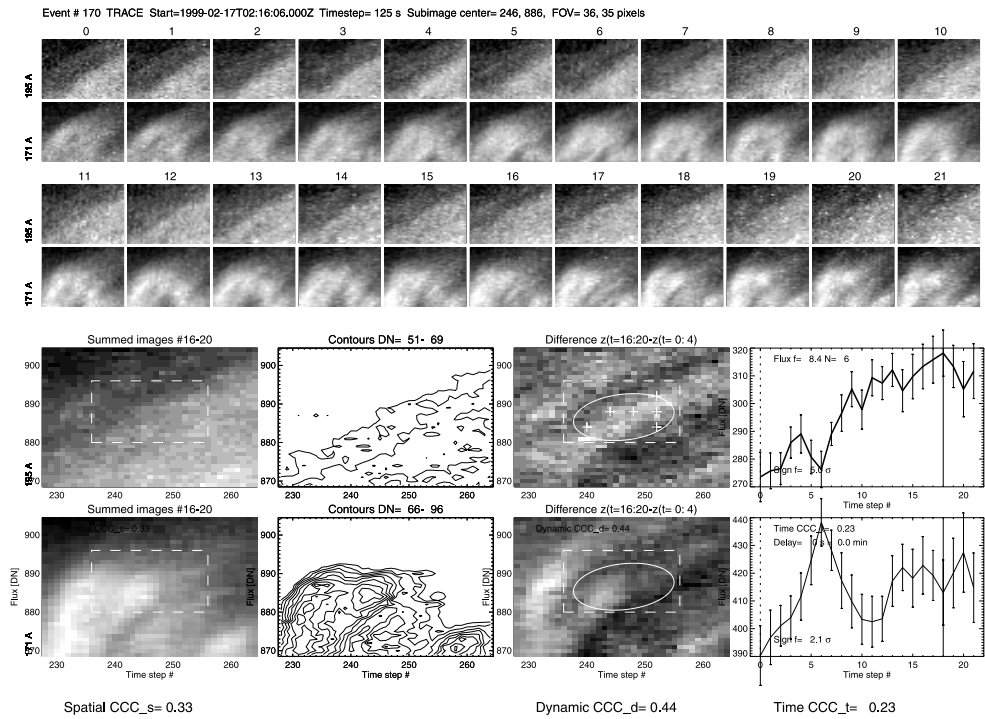


FIG. 10b

FIG. 10.—(a) Example of a flare event (no. 8), which is visible in both the 195 Å (first and third image sequence row) and the 171 Å data (second and fourth image sequence row). A sum image is shown as gray scale (bottom left) and contour plot (bottom second left). Difference images (bottom second right) show the difference between the peak time t_{peak} (no. 5) and the minimum time t_{min} (no. 16). The time profiles $F(t)$ (bottom right) are integrated over the area with variable pixels (marked with crosses in difference image). The error bars are calculated from the rms noise of the variable macropixels (eq. [17]). The spatial cross-correlation coefficient (calculated from the dashed box shown in the sum image) for this event is $\text{ccc}_s = 0.64$, the dynamic cross-correlation coefficient (calculated from the dashed box shown in the difference image) is $\text{ccc}_d = 0.76$, and the time cross-correlation coefficient (with a maximum at a delay of $\tau_{\text{delay}} = 3.6$ minutes) is $\text{ccc}_t = 0.94$ (see text on flare criterion, eq. [25]). (b) Example of an amorphous event (no. 170), in similar representation to that of (a). Note the low cross-correlation coefficients that disqualify this event from the flare list. (c) Example of a moss-associated event (no. 69), in a similar representation to that of (a). Note the reticulated moss structure in the 171 Å images, while a diffuse footpoint of a large-scale loop is visible in the 195 Å image. The temporal and spatial correlation is marginal.

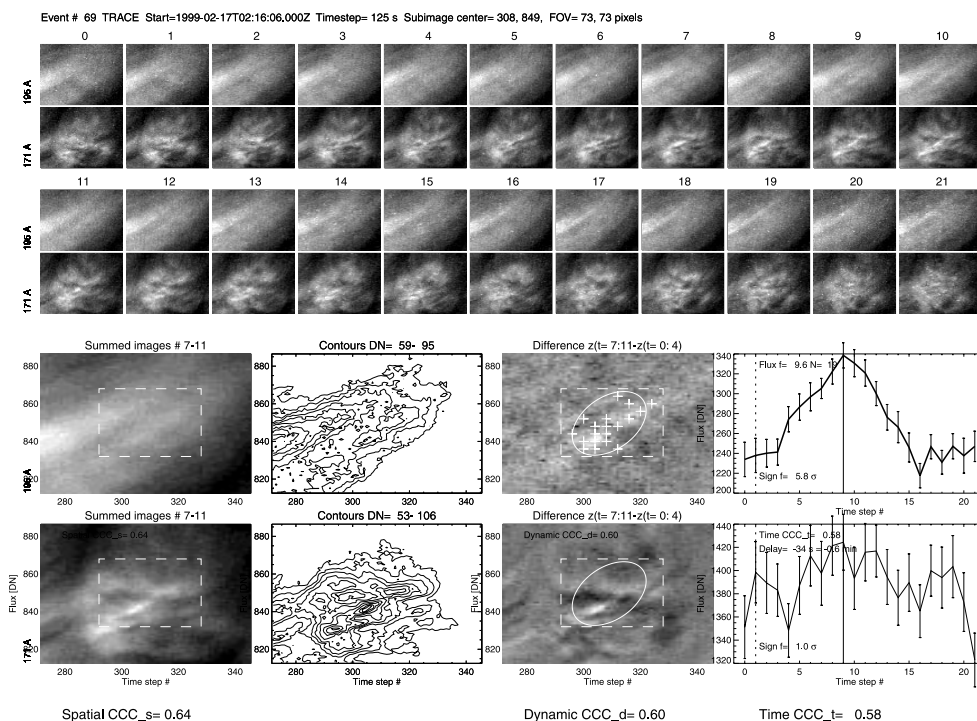


FIG. 10c

an elongated elliptical shape. The flare loops have a characteristic range of $l \approx 5000\text{--}20,000$ km and widths of $w \approx 2000\text{--}10,000$ km. (Note that the lower limits of spatial scales are given by the minimum area requirement of two macropixels, $l > 3$ Mm, $w > 1.5$ Mm.) These flare loops appear as compact sources, which have much smaller extents than the high-reaching coronal loops in active regions, that are often an order of magnitude larger. We identify a total of 319 (35%) flare events of the 904 events detected in 195 Å.

2. *Amorphous structures.*—In this category we put all events with significant variability that do not show well-defined compact flare loops. This category contains variable, diffuse large-scale structures, partial brightenings of large-scale loops, or unsharp structures due to insufficient signal-to-noise ratio. A possibility is also that moving large-scale loops mimic local brightness variations at their boundaries owing to the moving temperature or brightness gradients. An example is shown in Figure 10b. It is not clear whether a new loop at the edge of a large-scale structure brightens up, or if the edge of the large-scale loop is just moving without intrinsic brightness change. In contrast to flare events, time profiles at 171 and 195 Å are generally not correlated in amorphous events. We classify a total of 194 (21%) such amorphous events.

3. *“Moss”-associated structures.*—Observations of active regions with the TRACE 171 Å passband commonly reveal a bright, reticulated, low-lying emission pattern over magnetic plage regions, which have been dubbed “moss” because of their spongy appearance (Schrijver et al. 1999; Berger et al. 1999; Fletcher & DePontieu 1999). The cool (0.6–1.5 MK) “moss” structure is located in altitudes of ≈ 5000 km at the footpoints of hot 3–5 MK coronal large-scale loops (Berger et al. 1999). These findings strongly suggest that the moss is the high-temperature end of the transition region in which energy is conducted downward

through a steep temperature gradient (Schrijver et al. 1999). In this study, we find similar “mosslike” structure in the greater area of active regions or in areas surrounding coronal holes. The reticulated structure of the moss is best visible in the 171 Å images, while the 195 Å images generally show a diffuse cospatial structure, probably representing the footpoint of a hotter large-scale loop. It appears that many of these moss-associated variability events differ fundamentally from microflares because their time profiles show a much poorer correlation between 171 Å and 195 Å than flare events (Fig. 10c). We find a total of 62 (6%) moss-associated events.

4. *No structures.*—In this group we put all events that do not show any recognizable spatial structure in the sum or difference images, and have erratic time profiles. This group may contain events with noisy data: either random coincidences of noisy pixels that produce accidentally $\geq 3\sigma$ fluctuations in our detection scheme or nonrandom noise caused by some instrumental effects or residuals of cosmic-ray hits. They may also contain diffuse structures that are not obvious to the eye. We identify a total of 233 (25%) such featureless events.

5. *Bad data.*—This group comprises events that are obviously affected by bad data, e.g., bad (underefficient) pixels, temporarily hot pixels, data (telemetry) gaps, or obvious residuals of cosmic-ray hits. An obvious increase of cosmic-ray hits occurred around 14:42–14:46 UT when TRACE passed through one of the radiation belt zones. The chance coincidence of particle hits in identical pixels in subsequent images (or in corrupted neighbor pixels due to the *jpeg* compression) must have been higher during these times (image sequence no. 13–15) so that our time filter (eq. [3]) failed occasionally. These events have a high significance and compact sizes like flare events but can easily be recognized from their peak time (t_{peak} around sequence no. 14), their short duration, and uncorrelated behavior in 171 and

195 Å wavelengths. We identify a total of 95 (10%) of such events with bad data.

6.2. Quantitative Flare Classification Criterion

From the detailed visual inspection of all 904 events detected in the 195 Å images we learned that flare events often do show a highly correlated behavior at different temperatures, e.g., between 0.9 MK (171 Å) and 1.4 MK (195 Å), while nonflare events do not. It seems therefore to be a promising approach to use cross-correlation methods to establish sensitive criteria for a more objective and perhaps automated detection of flare events. For this purpose we calculate three types of temporal and spatial cross-correlation coefficients between the two temperatures.

A temporal cross-correlation coefficient ccc_t is calculated and maximized as function of the cross-correlation delay τ (within a time window of $\tau = \pm 2\Delta t$ in order to adjust for relative delays within ± 4 min),

$$ccc_t = \max [ccc(\tau)] = \max [\Delta F_{171}(t) \times \Delta F_{195}(t + \tau)], \quad (19)$$

where the net flux ΔF is integrated over an area that is covered by the significantly variable macropixels of an event (eq. [15]). In the same procedure we measure the relative cross-correlation delay τ , which is interpolated by a quadratic function within the discretized time steps Δt ,

$$\tau_{\text{Delay}} = \tau |_{\max [ccc(\tau)]} \approx t_{\text{peak}}(\Delta F_{171}) - t_{\text{peak}}(\Delta F_{195}). \quad (20)$$

A spatial cross-correlation coefficient ccc_s is calculated between the spatial flux distributions $f(x, y)$ at the two wavelengths,

$$ccc_s = \langle f_{171} \rangle(x, y, t_{\text{peak}}) \times \langle f_{195} \rangle(x, y, t_{\text{peak}}), \quad (21)$$

where $\langle f \rangle(x, y)$ represents a temporally averaged map around the peak time $t = t_{\text{peak}} \pm 2\Delta t$.

A dynamic (spatial) cross-correlation coefficient ccc_d is calculated between the changes of the spatial flux distributions $\Delta f(x, y)$ at the two wavelengths, which quantifies the correlated behavior of dynamic changes,

$$ccc_d = \langle \Delta f_{171} \rangle(x, y, t_{\text{peak}}) \times \langle \Delta f_{195} \rangle(x, y, t_{\text{peak}}) \quad (22)$$

$$\langle \Delta f_{171} \rangle(x, y, t_{\text{peak}}) = \langle f_{171} \rangle(x, y, t_{\text{peak}}) - \langle f_{171} \rangle(x, y, t_{\text{min}}) \quad (23)$$

$$\langle \Delta f_{195} \rangle(x, y, t_{\text{peak}}) = \langle f_{195} \rangle(x, y, t_{\text{peak}}) - \langle f_{195} \rangle(x, y, t_{\text{min}}). \quad (24)$$

Examples of these parameters ccc_t , ccc_s , ccc_d , and τ_{delay} can be seen for the three cases shown in Figures 10a–10c. The statistical distributions of these parameters are shown for each of the five event classes in Figure 11. From the histograms shown in Figure 11 (*left-hand panels*) it can be seen that about 90% of all flare events have a high temporal cross-correlation coefficient $ccc_t \geq 0.5$, a high spatial cross-correlation coefficient $ccc_s \geq 0.5$, and a high dynamic correlation coefficient $ccc_d \geq 0.5$, while all other event classes have generally lower values in the cross-correlation coefficients. The reason for the high cross-correlation coefficients in flare events suggests that flares have a relatively broad differential emission measure distribution $Q(T) = dEM(T)/dT$ and thus show a correlated evolution in nearby temperatures (e.g., in 0.9 and 1.4 MK of the 171 and 195 Å wavelengths). Further, we see that most of the flares reveal also a positive time delay of 171 Å with respect to the 195 Å wavelength (Fig. 11 [*top right*]), which can be explained as

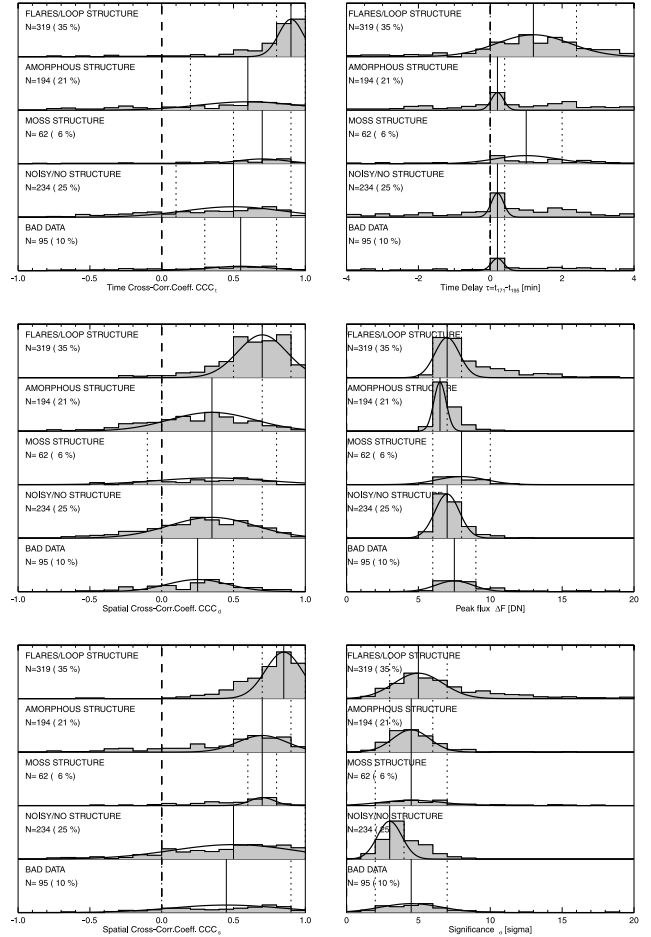


FIG. 11.—Distributions of the six parameters ccc_t , ccc_s , ccc_d , τ_{delay} , ΔF , and N_σ , separately shown for each of the five phenomenological classes. Note that flare events have the highest cross-correlation coefficients but do not differ much from other classes with respect to their flux ΔF or significance N_σ .

cooling delay of the 1.4 MK plasma down to the 0.9 MK temperature. However, we do not find much difference in the average flux ΔF or significance N_σ among the five event classes (Fig. 11 [*middle and bottom panels on right-hand side*]).

Given these preponderance of high cross-correlation coefficients in flare events we define now a quantitative flare criterion that consists of 3 (logical AND) conditions:

$$\text{FLARE CRITERION} = \begin{cases} ccc_t \geq 0.5 \\ ccc_s \geq 0.5 \\ ccc_d \geq 0.5. \end{cases} \quad (25)$$

We test now this quantitative criterion against our phenomenological classification performed for our 904 events detected in the 195 Å data cube (§ 6.1). In Table 3 we list how many events of every phenomenological class meets the flare condition defined in equation (25). If we define the success rate of our flare criterion by the ratio of events that are consistently classified visually and with the automated flare criterion (i.e., 222 flare events plus 526 nonflare events, marked with footnote a Table 3), of all classified (903) events, we obtain a success rate of 83%. In fact, because we do not know whether a fraction of amorphous or moss-associated events represent masked flares, the success rate

TABLE 3
TEST OF FLARE CRITERION VERSUS PHENOMENOLOGICAL CLASSIFICATION OF 195 Å EVENTS

Phenomenological Event Class	Flare Criterion Satisfied	Flare Criterion Not Satisfied
1. Flare events	222 (24.6%) ^a	97 (10.7%)
2. Amorphous events	14 (1.5%)	180 (19.9%) ^a
3. Moss-associated events	11 (1.2%)	51 (5.6%)
4. Structureless/noisy events	24 (2.7%)	210 (23.2%) ^a
5. Events with bad data	10 (1.1%)	85 (9.4%) ^a
All classes	281 (31.1%)	623 (68.9%)

^a Event classifications for which the flare criterion (eq. [25]) is consistent with phenomenological classes.

could be even higher. On the other hand, because a visual classification is always somewhat subjective, phenomenological classes should just be considered as a first guide with a grain of salt. The high consistency between the prediction of flare events and the visual verification of flare events encourages us to use the flare criterion established above (eq. [25]) as a valid criterion for automated flare searches.

We analyze the 171 Å data cube, in which a total of 3131 significant events have been recognized with our automated pattern recognition code, using now the automated flare

criterion (eq. [25]). We find that 798 (25.5%) of all (3131) significantly detected events in the 171 Å data fulfill our flare criterion. This is a similar percentage as in the 195 Å data, with 281 (31.1%) of 903 events. The absolute number of flares detected in 171 Å is, however, a factor of 2.8 larger, probably because there are more cooler ($T_e \lesssim 0.9$ MK) microflares than hotter ones ($T_e \approx 1.4$ MK).

6.3. Frequency Distributions of Flare Peak Fluxes $N(F)$

In Figure 12 we show the distributions $N(\Delta F)$ of peak fluxes ΔF . The peak flux ΔF represents the total flux increase integrated over the event area, which is the same quantity that is measured in time profiles $F(t)$ from instruments without spatial resolution, after subtraction of a pre- or postevent background, i.e., $\Delta F = F(t_{\text{peak}}) - F(t_{\text{min}})$ (when no coincident or time-overlapping events occur). We plot the frequency distribution or occurrence rate of events, $N(\Delta F)$, i.e., the number of events per bin (of the flux ΔF), in the customary form of a log N -log S histogram (Fig. 12). The distribution of all detected (904) events in 195 Å can be fitted with a power-law function $N(\Delta F) \propto F^{-a}$ with a slope of $a = 2.08$ (Fig. 12 [bottom]). However, if we separate the flare events, we find a significantly flatter slope, i.e., $a = 1.80 \pm 0.09$ for the subset of 319 visually identified flares, and a consistent value of $a = 1.85 \pm 0.05$ for the subset of 281 automatically detected flares (satisfying flare criterion eq. [25]). This result underscores the importance of a sensible classification scheme for variability events. The percentage of nonflare events seems systematically to increase with smaller fluxes ΔF , and thus steepens the power-law slope.

The flux distribution of events in the 171 Å data is shown in Figure 12 (top). This distribution cannot be fitted with a single power law. If we fit a double power law, we find a slope that varies from $a = 1.93$ at small fluxes to $a = 2.72$ at large fluxes. When we apply the automated flare criterion, we find for the subset of 798 flare events the same trend that the power-law slopes become flatter, i.e., varying from $a = 1.68$ to $a = 2.35$.

7. DISCUSSION

This study represents a first step toward a systematic analysis of microflaring in the solar corona. Microflaring has several interesting aspects. On one hand we would like to know whether microflares are operated by the same physical process as large flares and what the physical limits are for the smallest flares. On the other hand, the statistical aspects of microflares have far-reaching consequences regarding their energy budget that potentially could make up a significant fraction of the energy required to heat the corona. For both questions, it is of fundamental importance

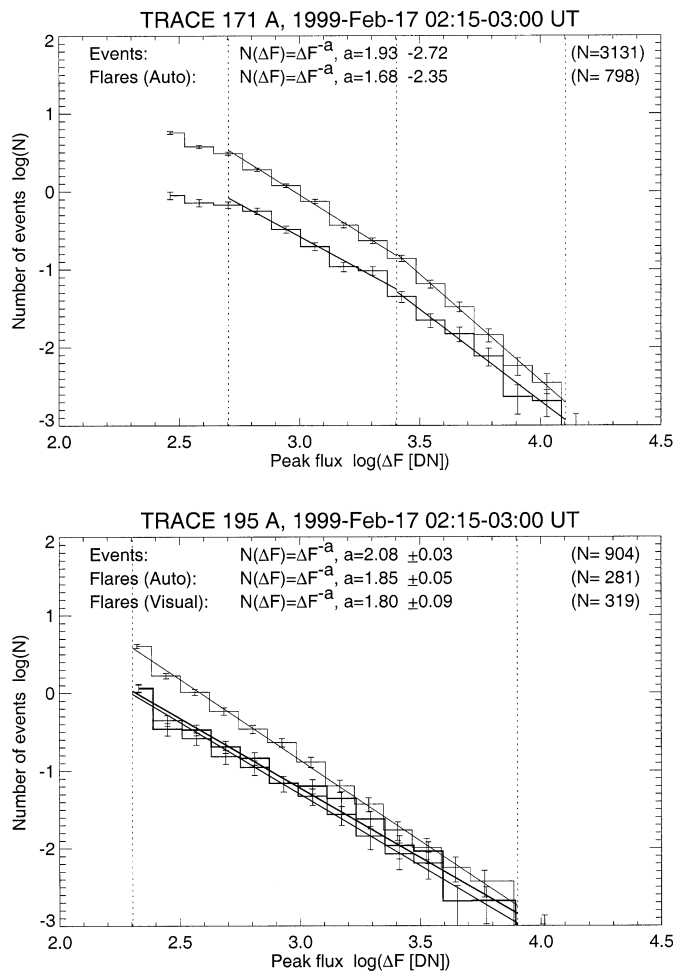


FIG. 12.—Frequency distributions of the peak flux ΔF for all events and subsets of flare events. At 195 Å two variants of flare subsets are shown, from the visual classification (Visual) and from the automated classification using flare criterion eq. (25) (Auto). The uncertainties in the power-law slope represent the formal errors of the linear regression fits. Note that the frequency distributions at 171 Å cannot be fitted by a single power law. A broken power-law fit is shown.

to establish a safe and objective criterion to distinguish microflare phenomena from numerous other time-variable fluctuations seen in the solar corona. To provide a solid basis for future studies, this paper is entirely dedicated to establish solid criteria to identify microflares at the lowest flux levels. In the following we discuss our findings in the context of other work, while the physical properties of microflares are the subject of Paper II (Aschwanden et al. 2000).

7.1. Defining Flare Events in EUV

The classical definition of a flare event originated from the observation of nonthermal particles via bremsstrahlung in hard X-rays and gyrosynchrotron emission in radio. A large fraction of the accelerated and emanating energetic particles necessarily bombard the chromosphere (owing to the preponderance of closed magnetic field lines in flare loop configurations) and drive chromospheric evaporation by local heating at the flare loop footpoints. This upflowing heated plasma is the brightest manifestation at soft X-ray wavelengths, and later in extreme ultraviolet (EUV), when it cools down to temperatures of 1–2 MK. From this canonical flare concept we can roughly predict what typical flare signatures in the 171 Å (Fe ix, 0.9 MK) and 195 Å (Fe xii, 1.4 MK) passband of *TRACE* should look like: The impulsive flare phase (with a duration of typically 1–2 minutes) should first show a rapid increase of the 195 Å flux during a few minutes, followed by an exponential decay due to the flare plasma cooling with a typical cooling time of a few minutes to hours, depending on the density (which controls the radiative cooling time) or temperature gradient (which controls the conductive cooling time) of the flare loop. Because the flare loop cooling phase is generally longer than the preceding impulsive heating phase, the peak of the EUV emission in the 171 Å passband should peak somewhat later than the 195 Å peak. The relative time delay corresponds to the time interval during which the bulk of the flare plasma cools down from 1.4 to 0.9 MK. This scenario is largely confirmed by our analysis of 171 and 195 Å observations of flare events in *TRACE* data. In simple events we see a rise time of 2–4 minutes and an exponential decay during typically 3–30 minutes, with a relative time delay of about a minute between the 195 and the 171 Å peak (e.g., Fig. 10a). If the EUV emission during a flare event comes from the cooling plasma of a single flare loop, we expect that the time profiles at two nearby temperatures should be highly correlated, which is indeed the case for the majority of flare events in which we detected a single loop in the *TRACE* images. Based on this consistency between theoretically expected EUV signatures in nearby temperatures and the observed features in the 171 and 195 Å passbands, we are led to adopt spatial and temporal cross-correlation coefficients between the two temperature bands as a well-justified physical criterion to distinguish flare events from other dynamic phenomena.

A question is, however, whether our flare criterion rejects true flare events that do not meet our cross-correlation criterion. Table 3 shows that 97 visually classified flare events do not meet the flare criterion (a fraction of 10.7% of the entire data set). This misidentified events consist mainly of flare events with a poorer spatial correlation. If we relax the cross-correlation coefficient requirements by a factor of 2 (i.e., $ccc_t > 0.25$, $ccc_s < 0.25$, $ccc_d < 0.25$), the number of rejected flares can be reduced to one-third, down to 36

(4.0% of the data set), however at the expense of more accepted nonflare events, resulting in an overall lower success rate of 74.0% (measured by the consistency with visually classified flares). Our flare criterion has therefore to be considered as an optimized compromise between flare acceptance and nonflare rejection, but has soft limits, say within $0.25 \lesssim ccc \lesssim 0.5$. Investigating further the remaining misidentified 36 flare events with (one of the) $ccc < 0.25$ we find that the main reason for a poor correlative behavior comes mainly from confusion by adjacent dynamic activities that cannot be properly separated in space and time. Potentially, there is also the possibility that cooler flares with a maximum temperature of $T_e \approx 1$ MK are detected in the 171 Å waveband, but not in the 195 Å waveband. Our statistics indicate that there is a larger number of cooler flares (798 flare events detected in 171 Å vs. 281 flare events detected in 195 Å). However, the overlap of the 195 Å response function with the peak temperature of the 171 Å passband seems to be sufficient to pick up about 10% of the emission measure seen at 0.9 MK, the center of the 171 Å passband. This provides in most of the cases sufficient counts here to ensure a high cross-correlation coefficient between the two temperatures, though with less significance in the 195 Å data.

Conversely, we may ask whether our flare criterion could be fooled by nonflaring phenomena that exhibit a highly correlated behavior in nearby temperatures. Table 3 shows that the rejection of nonflare events is fairly rigorous: Only one of 14 amorphous events, or one of six moss-associated events, or one of 10 structureless events, or one of 10 bad data events is misidentified as flare event. Totally, only 6.5% of the data set represent nonflare events that are misidentified as flare events. If we would relax the flare criterion to $ccc > 0.25$, the fraction of misidentified flare events would rise from 6.5% to 22%.

Despite the total uncertainty of 17% of our flare classification criterion (with a probability of 10.7% to reject flare events and 6.5% to accept nonflare events), this uncertainty seems not to introduce a bias in the flare occurrence rate as function of the EUV flux. The frequency distribution shown in Figure 12 shows that the difference in the power-law slope is comparable to the formal error of the fit, i.e., $a = 1.80 \pm 0.09$ for the subset of visually classified flares versus $a = 1.85 \pm 0.05$ for the subset of automatically classified flares.

7.2. Frequency Distributions of Flare EUV Peak Fluxes

The (background-subtracted) peak flux ΔF of a flare represents the simplest and most direct observable parameter that quantifies the magnitude of a flare, which can be measured even from time profiles of nonimaging instruments. Most of the published frequency distributions from flares are therefore based on the peak flux (see compilation in Table 1 of Aschwanden, Dennis, & Benz 1998) and thus can be directly compared with our statistics obtained here. Frequency distributions of flare energies, which are more important with regard to energy budget considerations (e.g., to heat the solar corona), require the determination of electron densities, which is model dependent and will be derived and modeled in Paper II.

The frequency distribution of the EUV peak flux ΔF of flares detected in 195 Å (Fe xii, 1.4 MK) can be fitted with a power law over a range of 1.6 decades dynamic range in flux (a factor of 40 between the largest and smallest detected

microflare). The power-law slope of the distribution $N(\Delta F) \propto \Delta F^{-a}$ is found to be $a = 1.83 \pm 0.07$, if we take the weighted mean of the two values found from both methods (i.e., flare identification by visual inspection vs. automated detection). This value is consistent with power-law slopes found from hard X-ray peak fluxes (e.g., $a = 1.8$ – 1.9 , Dennis 1985; $a = 1.67$ – 1.73 , Crosby, Aschwanden, & Dennis 1993; $a = 1.86$ – 2.00 , Bromund, McTiernan, & Kane 1995), or with soft X-ray microflares (e.g., $a = 1.75$, Drake 1971; $a = 1.79$ – 1.86 , Lee, Petrosian, & McTiernan 1995) and soft X-ray brightenings (e.g., $a = 1.68$ – 1.80 , Shimizu 1995; Shimojo & Shibata 1999). For EUV emission of flares, frequency distributions have been published only recently. Berghmans et al. (1998) find a value of $a = 1.35 \pm 0.2$ for coronal events detected in 195 Å with *SOHO*/EIT (according to their Fig. 25, where the radiative loss per event is defined to be proportional to the EUV flux ΔF at 195 Å). This value appears to be significantly lower than that found here, but their frequency distribution also shows substantial deviations from a power-law function and thus inherently bears an ill-defined power-law slope. Krucker & Benz (1998), in contrast, find a significantly steeper slope of $a = 2.3$ – 2.6 for the thermal energy E_{th} in microflares simultaneously detected in 171 Å and 195 Å with *SOHO*/EIT. However, these values cannot directly be compared with the distributions of the peak flux ΔF here because the computation of the thermal energy E_{th} is model dependent (i.e., assumptions on isothermality to infer a filter-ratio temperature; assumptions on loop widths and column depths to convert an emission measure into electron density). The conversion of observed EUV parameters into physical energy units and the resulting frequency distributions of EUV flare energies is the subject of Paper II. At this point, in spite of the diverging results of power-law slopes for EUV flare energies published recently, we just note that the frequency distributions of the most directly observable parameter, i.e., the peak flux ΔF , shows at 195 Å (1.4 MK) a frequency distribution that is compatible with previous results from soft X-ray and hard X-ray peak fluxes of flares.

At cooler EUV temperatures, namely at $T_e = 0.9$ MK (171 Å), however, we find a frequency distribution of peak fluxes ΔF that cannot be fitted with a single power law (Fig. 12 [top]). If we fit a two-component power law, we find a slope of $a \approx 1.7$ for weak fluxes [$\log(\Delta F) = 2.5$ – 3.4], and a steeper slope of $a \approx 2.4$ for higher fluxes [$\log(\Delta F) = 3.4$ – 4.1]. This deviation from a single power law seems not to be an effect of the automated flare classification criterion because similar double slopes are also found for all events without discrimination of flares ($a \approx 1.9$ – 2.7 Fig. 12 [top]). The discrimination of flare events merely flattens both slopes by about $\Delta a = -0.2$, similar to the 195 Å data. At this point it would be premature to interpret the flattening of the power-law slope at low flux values; it could be due to a systematic undersampling effect or a side effect in the breakdown of spatiotemporal structures with our pattern recognition code, or it could be related to a real physical reason related to small cool flares at temperatures $T_e \lesssim 1.0$ MK (e.g., increased absorption for small-scale flare loops immersed in the chromosphere below the transition region zone; see Aschwanden 2000).

8. CONCLUSIONS

The purpose of this study is to analyze the time variability of EUV emission from the quiet Sun, to correct for

instrumental effects that contribute to artificial time variability, and to identify from the remaining variability attributable to true solar phenomena those events that are associated with microflares. With this task we aim to establish a firm basis for pursuing statistics and analysis of physical parameters of EUV microflares in subsequent studies. The findings can be summarized as follows:

1. Using *TRACE* 171 and 195 Å images with relatively long exposures, we find that artificial variability is caused by “bad” (underefficient) pixels, “hot” (temporarily enhanced) pixels, orbit-correlated spacecraft temperature variations that affect the readout pedestal value or readout noise, spacecraft pointing drift on the order of $\lesssim 2''$, and mostly by radiation spikes caused by cosmic-ray hits, even after correction with a local filter function, because there remain small residuals in neighbor pixels due to the on-board *jpeg* data compression algorithm. Pixel defects (bad and hot pixels) introduce time variability because they move in an image that does not track solar rotation. After identification and correction of all known effects we find that the dominant source of data noise consists of residuals from cosmic-ray hits, while photon Poisson noise is much less severe. The rate of cosmic-ray hits is much higher for the *TRACE* spacecraft (which passes through radiation belt zones) than for the *SOHO*/EIT instrument operating at the same wavelengths (located in the Lagrangian point far away from the Earth’s radiation belt).

2. During an observing interval of 45 minutes with a cadence of 2 minutes we find that $\approx 50\%$ of the quiet-Sun field of view shows significant $\geq 3\sigma$ variability at 171 Å and $\approx 15\%$ at 195 Å. We measured the variability within 4×4 macropixels to improve the signal-to-noise ratio and to eliminate spacecraft pointing drift $\lesssim 2''$.

3. We developed a spatiotemporal pattern recognition code which assembles time-variable macropixels with a size of $2''$ and a time coincidence of ± 2 minutes. This algorithm organizes the spatiotemporal events into 3131 significant events in 171 Å and 904 events in 195 Å.

4. Inspecting the images and time profiles of significant events we identify 319 (35%) events with flarelike characteristics (brightening and dimming loops) in the 195 Å data. We quantify a numerical flare criterion based on high cross-correlation coefficients ($\text{ccc} > 0.5$) in time profiles, spatial maps, and dynamic changes of spatial maps between the two (peak) temperatures (0.9 and 1.4 MK) of the 171 and 195 Å passband. We establish that this numerical flare criterion matches the visual classification in 83% of the cases. Applying this automated flare criterion we find a total of 281 microflares in the 195 Å data and 798 microflares in the 171 Å data.

5. The frequency distribution of flare peak fluxes can be fitted with a power law with a slope of $a = -1.83 \pm 0.07$ at 195 Å, which is in good agreement with SXR and HXR flare peak fluxes. The application of a flare discrimination criterion is found to be very important to derive the correct power-law slope of a flare frequency distribution. Neglect of flare discrimination would lead to power-law slopes that are steeper by $\Delta a = +0.3$ in both the 171 and 195 Å wavelengths.

In the second paper of this series we will characterize the physical parameters of the EUV microflares detected and discriminated with the method described here. Some of the detected microflares show a very simple spatial structure

and highly correlated temporal evolution in nearby temperatures and are therefore suitable for simple modeling of heating and cooling processes. From this modeling we anticipate deriving their energy input in a reliable way that allows us to build up statistics on microflare energetics that ultimately may shed light on the issue whether microflares have the required spatial distribution and occurrence rate to heat the solar corona.

This work was supported by contract NAS5-38099 and NAS8-40108. We appreciate helpful discussions with

Arnold Benz, Säm Krucker, and Clare Parnell. We thank Alan Title, Karel Schrijver, and *TRACE* planner Ed DeLuca for support and execution of the *TRACE* observations analyzed here. We acknowledge also helpful discussions, software support, and assistance in data processing from the *TRACE* team. The *TRACE* team includes scientists from Lockheed Martin Advanced Technology Center, Stanford University, NASA Goddard Space Flight Center, the University of Chicago, Montana State University, and the Harvard-Smithsonian Center for Astrophysics.

REFERENCES

- Aschwanden, M. J. 2000, *Sol. Phys.*, in press
 Aschwanden, M. J., Dennis, B. R., & Benz, A. O. 1998, *ApJ*, 497, 972
 Aschwanden, M. J., Tarbell, T. D., Nightingale, R. W., Schrijver, C. J., Title, A., Kankelborg, C. C., Martens, P., & Warren, H. P. 2000, *ApJ*, 535, 1047 (Paper II)
 Benz, A. O., & Krucker, S. 1998, *Sol. Phys.*, 182, 349
 ———, 1999, *A&A*, 341, 286
 Berger, T. E., De Pontieu, B., Schrijver, C. J., & Title, A. M. 1999, *ApJ*, 519, L97
 Berghmans, D., Clette, F., & Moses, D. 1998, *A&A*, 336, 1039
 Bromund, K. R., McTiernan, J. M., & Kane, S. R. 1995, *ApJ*, 455, 733
 Chae, J., Qiu, J., Wang, H., & Goode, P. R. 2000, *ApJ*, 528, L119
 Crosby, N. B., Aschwanden, M. J., & Dennis, B. R. 1993, *Sol. Phys.*, 143, 275
 Dennis, B. R. 1985, *Sol. Phys.*, 100, 465
 Drake, J. F. 1971, *Sol. Phys.*, 16, 152
 Fletcher, L., & DePontieu, B. 1999, *ApJ*, 520, L135
 Freeland, S. L., & Handy, B. N. 1998, *Sol. Phys.*, 182, 497
 Handy, B., et al. 1999, *Sol. Phys.*, 187, 229
 Krucker, S., & Benz, A. O. 1998, *ApJ*, 501, L213
 Lee, T. T., Petrosian, V., & McTiernan, J. M. 1995, *ApJ*, 418, 915
 Porter, J. G., Fontenla, J. M., & Simnett, G. M. 1995, *ApJ*, 438, 472
 Porter, J. G., Moore, R. L., Reichmann, E. J., Engvold, O., & Harvey, K. L. 1987, *ApJ*, 323, 380
 Schrijver, C. J., et al. 1999, *Sol. Phys.*, 187, 261
 Shimizu, T. 1995, *PASJ*, 47, 251
 Shimojo, M., & Shibata, K. 1999, *ApJ*, 516, 934
 Tarbell, T. D., et al. 1994, in *Proc. 3rd SOHO Workshop—Solar Dynamic Phenomena and Solar Wind Consequences (ESA SP-373)* (Paris: ESA), 375
 Wang, H., Chae, J., Qiu, J., Lee, C. Y., & Goode, P. R. 1999, *Sol. Phys.*, submitted